

Radio-Excess *IRAS* Galaxies: PMN/FSC Sample Selection

Catherine L. Drake^{1,2}, Peter J. McGregor¹, Michael A. Dopita¹,

and

W. J. M. van Breugel³

cdrake,peter,mad@mso.anu.edu.au,vanbreugel1@l1nl.gov

ABSTRACT

A sample of 178 extragalactic objects is defined by correlating the 60 μm IRAS FSC with the 5 GHz PMN catalog. Of these, 98 objects lie above the radio/far-infrared relation for radio-quiet objects. These radio-excess galaxies and quasars have a uniform distribution of radio excesses with no evidence for a radio-loud correlation equivalent to the well known radio-quiet radio/far-infrared relation. The radio-intermediate objects appear to be a new population of active galaxies not present in previous radio/far-infrared samples chosen using more stringent far-infrared criteria. The radio-excess objects extend over the full range of far-infrared luminosities seen in extragalactic objects, from low luminosity galaxies with $\nu L_\nu(60 \mu\text{m}) < 10^9 L_\odot$ to ultra-luminous infrared galaxies with $\nu L_\nu(60 \mu\text{m}) > 10^{12} L_\odot$. Objects with small radio excesses are more likely to have far-infrared colors similar to starbursts, while objects with large radio excesses have far-infrared colors typical of pure AGN. Some of the most far-infrared luminous radio-excess objects have the highest far-infrared optical depths. These are good candidates to search for hidden broad line regions in polarized light or via near-infrared spectroscopy. Some low far-infrared luminosity radio-excess objects appear to derive a dominant fraction of their far-infrared emission from star formation, despite the dominance of the AGN at radio wavelengths. Many of the radio-excess objects have sizes likely to be smaller than the optical host, but show optically thin radio emission, rather than flat radio spectra indicative of compact quasar cores. We draw parallels between these objects and high radio luminosity Compact Steep-Spectrum (CSS) and GigaHertz Peaked-Spectrum (GPS) objects. Radio sources with these characteristics may be young AGN in which the radio activity has begun only recently. Alternatively, high central densities in the host galaxies may be confining the radio sources to compact sizes. We discuss future observations required to distinguish between these possibilities and determine the nature of radio-excess objects.

Subject headings: galaxies: active — galaxies: Seyfert — infrared: galaxies — radio continuum: galaxies — surveys

1. Introduction

Active galaxies have traditionally been separated into radio-quiet and radio-loud classes (Miller, Peacock, & Mead 1990). Radio-quiet objects include starburst galaxies, Seyfert galaxies, and radio-quiet quasars. Radio-loud objects include radio galaxies and radio-loud quasars. The radio-quiet objects

¹Research School of Astronomy and Astrophysics, The Australian National University, Cotter Rd, Weston, ACT 2611 Australia

²Australia Telescope National Facility, PO Box 76, Epping, NSW 1710 Australia

³Institute of Geophysics and Planetary Physics, Lawrence Livermore National Laboratory, L-413, P.O. Box 808, Livermore, CA 94550

follow a remarkably tight correlation between their 60 μm far-infrared (FIR) and GHz radio continuum luminosities (van der Kruit 1973; Rickard & Harvey 1984; Dickey & Salpeter 1984; de Jong et al. 1985; Helou, Soifer, & Rowan-Robinson 1985; Condon & Broderick 1986; Wunderlich, Klein, & Wielebinski 1987; Condon & Broderick 1988; Walsh et al. 1989; Condon, Anderson, & Helou 1991a; Sopp & Alexander 1991; Cram, North, & Savage 1992), although Seyfert galaxies and radio-quiet quasars appear to scatter somewhat more than starburst galaxies (Sanders & Mirabel 1985; Condon & Broderick 1988; Baum et al. 1993). The correlation is attributed to stellar processes that are thought ultimately to be responsible for both the radio and the FIR emission. Radio-loud objects lie up to ~ 3 dex in radio luminosity above the starburst line. Their radio emission is clearly associated with an active nucleus. A radio/FIR correlation has been suggested for radio-loud objects, but with significantly more scatter than for radio-quiet objects (Sopp & Alexander 1991). The lower edge of this relation, at least at 5 GHz, corresponds approximately with the equivalent flux limit of the 408 MHz revised 3C radio catalog (Bennett 1963), suggesting that it may be an artifact of the sample selection rather than having a physical basis.

It has recently become apparent that a class of objects exists with intermediate radio properties. Dey & van Breugel (1994) correlated the 60 μm *IRAS* Faint Source Catalog (FSC) with the Texas 365 MHz radio survey and identified objects lying at intermediate radio luminosities in the radio/FIR diagram. Many of these objects have optical spectra with features characterized as post-starburst AGN; strong Balmer absorption lines and Seyfert 2 emission lines ([O III] $\lambda 5007$ stronger than $\text{H}\alpha$) or LINER-like emission lines ([O II] $\lambda 3727$ stronger than [O III] $\lambda 5007$, [O I] $\lambda 6300$ /[O III] $\lambda 5007 > 0.3$; Heckman 1980). Condon, Anderson, & Broderick (1995, hereafter CAB) correlated the 60 μm *IRAS* FSC with the Greenbank 4.8 GHz radio survey and identified a similar sample of radio-excess galaxies, although they did not explicitly comment on this. The radio-intermediate objects in their sample encompass a range of FIR luminosities⁴ from low luminosity systems with $L_{\text{FIR}} \sim 10^8 L_{\odot}$ to highly luminous infrared galaxies with $L_{\text{FIR}} \geq 10^{11} L_{\odot}$. Subsequently, Roy & Norris (1997) showed that selecting FIR luminous galaxies that have a radio excess is an effective method of finding dusty, gas-rich active galactic nuclei (AGN). More recently, Yun, Reddy, & Condon (2001) correlated *IRAS* FSC sources above 2 Jy at 60 μm with the NRAO *VLA* Sky Survey (Condon et al. 1998, NVSS) at 1.4 GHz, and identified a small number of radio-intermediate objects (23 of 1809). Corbett et al. (2002) have also identified a small number of radio-intermediate objects in their sample of low power AGN.

Ultra-luminous infrared galaxies (ULIRGs) feature among the most FIR luminous radio-intermediate objects⁵. Most ultra-luminous infrared galaxies are in interacting or recently merged systems (Soifer, Houck, & Neugebauer 1987), and include both starburst galaxies and AGN. Indeed, both types of activity coexist in many ultra-luminous infrared galaxies. This supports the idea that galaxy interactions trigger intense nuclear starbursts that may evolve into AGN activity (Sanders et al. 1988a,b). Multiple nuclei are common, suggesting that the progenitors of many ultra-luminous infrared galaxies may be compact groups of galaxies (Borne et al. 2000). Radio-intermediate infrared-luminous galaxies share some of these characteristics and so may be relevant to studies of how AGN activity is initiated.

The radio emission from radio-intermediate ultra-luminous infrared galaxies may arise in several ways. At one extreme, they may be “weak” radio galaxies that will never achieve radio luminosities commensurate with those of 3C radio galaxies and quasars. At the other extreme, they may be dusty, gas-rich systems in which the radio activity is not yet fully developed because the nascent radio jet has only just started to emerge in the confining interstellar medium (ISM) of the host galaxy. Radio-intermediate ultra-luminous infrared galaxies may therefore share some similarities with compact steep-spectrum (CSS)

⁴The FIR luminosity is estimated from the FIR flux density $S_{\text{FIR}} = 1.26 \times 10^{-14} (2.58 S_{\nu}(60 \mu\text{m}) + S_{\nu}(100 \mu\text{m})) \text{ Wm}^{-2}$ (Sanders & Mirabel 1996).

⁵Luminous infrared galaxies are defined formally to have $10^{11} < L_{\text{FIR}} < 10^{12} L_{\odot}$ and ultra-luminous infrared galaxies are defined to have $L_{\text{FIR}} > 10^{12} L_{\odot}$ (Sanders & Mirabel 1996).

and GigaHertz peaked-spectrum (GPS) radio sources (O’Dea 1998). CSS radio sources are objects in which the radio lobes are contained within the ~ 15 kpc extent of the host galaxy and the radio emission is optically thin, unlike the flat-spectrum cores of radio galaxies and radio-loud quasars (Fanti et al. 1990; De Young 1993; Gelderman & Whittle 1994; Fanti et al. 1995). GPS sources are believed to be similar to CSS objects, but with scales of < 1 kpc. CSS and GPS sources have steep radio spectra at high radio frequencies, but the spectra of GPS sources turn over around 1 GHz and decline with decreasing frequency, whereas the spectra of CSS sources continue to rise (O’Dea 1990; O’Dea et al. 1990; O’Dea, Baum, & Stanghellini 1991; O’Dea et al. 1996). This turnover may be due to free-free absorption (FFA) in material surrounding the radio lobes (e.g., Bicknell, Dopita, & O’Dea 1997) or to synchrotron self-absorption (SSA) in the emitting plasma (e.g., Readhead et al. 1996). CSS/GPS radio sources may be young (Fanti et al. 1995), or the interstellar medium of the host galaxy may be sufficiently dense to confine the radio plasma (van Breugel 1983).

In this paper, we define a sample of radio-excess infrared galaxies based on source detections in the $60 \mu\text{m}$ *IRAS* FSC and the Parkes-MIT-NRAO (PMN) 4.8 GHz point source catalog. This sample is combined with similar CAB objects in an attempt to better determine the nature of radio-excess objects. Our cross-correlation of the catalogs and subsequent observations are described in §2. Results for the full sample of radio-quiet and radio-excess objects are presented in §3 where we also define a radio-excess sub-sample. The nature of these radio-excess objects is explored in §4 by noting the many well-studied objects in the sample. The properties of the radio-excess sample as a whole are considered in §5 where we highlight similarities with CSS/GPS sources. Our conclusions are summarized in §6. We adopt $H_0 = 50 \text{ km s}^{-1} \text{ Mpc}^{-1}$ and $q_0 = 0.5$ throughout.

2. Radio-*IRAS* Identifications

2.1. Cross-Correlations

The PMN/FSC sample is based on a cross-correlation of the Parkes-MIT-NRAO (PMN) 4.8 GHz catalog with $60 \mu\text{m}$ detections in the *IRAS* FSC. The PMN survey covered the whole sky between declinations $+10^\circ$ and -87° to a 4.8 GHz flux density limit of typically ~ 30 mJy, rising to ~ 45 mJy in equatorial regions (Griffith & Wright 1993; Griffith et al. 1994; Wright et al. 1994; Griffith et al. 1995; Wright et al. 1996). The catalog derived from these data has a positional accuracy of $\sim 10''$ for bright sources, and falls to $\sim 40''$ at the flux density limit of the survey (Griffith & Wright 1993). The *IRAS* FSC (Moshir et al. 1992) at $60 \mu\text{m}$ covers 94% of the sky with $|b| \geq 10^\circ$ to a flux density limit of ~ 200 mJy and a positional uncertainty typically of $\sim 7'' \times 25''$. We require an *IRAS* detection only at $60 \mu\text{m}$ for inclusion in our sample. Hence we have considered more candidate objects than previous samples that have been based on *IRAS* color selection (e.g., CAB; Roy & Norris 1997; Yun et al. 2001). This leads to the inclusion of a larger number of faint *IRAS* detections in our sample.

The cross-correlations were performed using the XCATSCAN facility at the Infrared Processing and Analysis Center⁶ (IPAC). Initially, all sources with PMN positions within $60''$ of an *IRAS* position were accepted. Correlations with Galactic objects such as stars, star clusters, planetary nebulae, and H II regions were then removed, as were correlations in the direction of the Magellanic Clouds. The resulting sample consisted of 279 radio/FIR correlations. The NASA/IPAC Extragalactic Database⁷ (NED) was

⁶IPAC is operated by the Jet Propulsion Laboratory, California Institute of Technology, under contract with the National Aeronautics and Space Administration.

⁷NED is operated by the Jet Propulsion laboratory, California Institute of Technology, under contract with the National Aeronautics and Space Administration

then searched for data on each correlation. Many correlations correspond to bright galaxies for which the radio/FIR association is unquestioned. Others correspond to fainter galaxies or quasars with previously measured redshifts, while the remainder either correspond to objects with unknown redshifts that are faint on Digitized Sky Survey⁸ (DSS) images or for which the optical identification is confused.

2.2. Valid Correlations

We now consider whether each of the 279 correlations is a valid association of the FIR and radio sources. In general, the PMN radio positions are not of sufficient accuracy to allow us to make unambiguous associations with FIR sources or to assign optical identifications based solely on positional coincidence. We therefore used information from the literature and new observations to improve the radio positional accuracy for each correlation. We adopt as our criterion for acceptance of a radio/FIR correlation in the final sample that the accurate (i.e., $< 5''$) radio position lies within the *IRAS* FSC 60 μm 3σ error ellipse.

A number of more accurate radio positions were available from the literature. CAB have performed a similar selection in the northern hemisphere in the region $0^h < \alpha < 20^h$ and $\delta > -40^\circ$. They list 4.8 GHz positions with $\sim 1''$ uncertainty measured from *VLA* snapshots for 58 of our radio/FIR correlations. Accurate 1.4 GHz radio positions ($\sim 1''$) are also available from the NVSS (Condon et al. 1998) for a further 127 of our correlations north of declination -40° . The NVSS data confirm 116 of these radio/FIR correlations, while 11 correlations were rejected on the basis that the nearest 1.4 GHz radio source lies outside the *IRAS* 3σ error ellipse.

Snapshots at 3 cm and 6 cm were obtained with the Australia Telescope Compact Array (*ATCA*) for 54 southern correlations. Observations were made in 1996 July and 1998 January using the 6C configuration and in 1998 February using the 6B configuration. Both configurations have a maximum baseline of 6 km. Antenna 2 was out of operation during the 1998 January observing run, resulting in the loss of 5 baselines, including the shortest one (153 m). Sources were observed at 8.64 GHz and 4.79 GHz with a bandwidth of 128 MHz. Unlike the *VLA*, the *ATCA* is a linear E-W array of six 22 m dishes so several observations of each object at different hour angles (i.e., cuts) were required to minimally sample the $u-v$ plane. Generally 6 cuts of 3 minutes each were obtained for each object, evenly spaced in time while the object was accessible above the horizon. A phase calibrator was observed within ~ 20 minutes in time and $\sim 10^\circ$ in angle on the sky of each group of 1–6 target sources. The *ATCA* primary calibrator, PKS B1934-638, was observed during each session to calibrate flux densities.

The data were reduced using *MIRIAD* (Sault, Teuben, & Wright 1995). Bad data were flagged and data from all observing dates were combined. MFCAL was used to flux calibrate the visibilities relative to PKS B1934-638, which is assumed to have flux densities of 2.842 Jy and 5.843 Jy at 8.64 GHz and 4.79 GHz, respectively. Phase solutions were calculated for the secondary calibrators using GPCAL then phase calibration was applied to the target sources using GPCOPY. Maps of target sources were made and cleaned using MFCLEAN. Cleaned maps were restored using a Gaussian beam with uniform weighting. All but two sources were self-calibrated; self-calibration was omitted for one source because it is too faint and for another because it is too extended. Total integrated fluxes were measured using IMFIT in *MIRIAD*. These are listed in Table 1. Flux density limits (3σ) at the two frequencies are typically ~ 1.7 mJy beam⁻¹ and ~ 1.2 mJy beam⁻¹, respectively. The beam is approximately circular for most sources, with a FWHM of $\sim 1''$ at 8.64 GHz and $\sim 2''$ at 4.79 GHz. For sources approaching

⁸DSS, The Digitized Sky Survey was produced at the Space Telescope Science Institute under U.S. Government grant NAG W-2166. The images of these surveys are based on photographic data obtained using the Oschin Schmidt Telescope on Palomar Mountain and the UK Schmidt Telescope.

the northern limit of the *ATCA* of $\sim -10^\circ$ declination, the beam is progressively more elongated in the North-South direction up to $\sim 90''$ in extreme cases. The errors in the measured source positions are estimated to be $\sim 1\text{--}5''$ with the larger values in this range applying to the more northern sources that have elongated beams. This positional accuracy is adequate for confirming radio/FIR correlations and assigning optical identifications in unconfused regions.

The *ATCA* observations confirmed 28 of the radio/FIR correlations, while the radio source was either not detected or was deemed not to be associated with the FIR source in a further 26 correlations.

Optical counterparts to the radio sources were then sought on Digitized Sky Survey images. In many cases, only one optical object is present in the *IRAS* 3σ error ellipse and this is confirmed to be the radio object. However, when more than one optical object is present in the *IRAS* 3σ ellipse, this procedure leaves uncertain whether the radio/optical object is also the FIR source. These cases were deemed to be uncertain FIR identifications and were rejected. A total of 24 correlations were excluded due to this optical confusion.

The final sample of 178 objects are confident associations of PMN radio sources with *IRAS* FSC $60\ \mu\text{m}$ sources. These 178 objects are listed in Table 1. Column 1 lists the *IRAS* name. Column 2 lists the PMN name. Columns 3 and 4 list the J2000 source position. Column 5 indicates the origin of the source position; positions from Condon et al. (1995) are listed as CAB, positions from the NVSS are listed as NVSS, positions from our *ATCA* snapshots are listed as ATCA, PMN positions are listed as PMN and positions derived from the optical host galaxies measured from DSS images are listed as DSS. Columns 6 and 7 list the *IRAS* $25\ \mu\text{m}$ and $60\ \mu\text{m}$ flux densities; except where noted, fluxes are from the FSC. Columns 8 and 9 list the 8 GHz and 5 GHz flux densities, respectively. Column 10 lists the origin of the 5 GHz flux density as either our *ATCA* snapshots or the PMN catalog. The single-dish PMN measurements suffer from source confusion so their flux densities at low levels can be unreliable. Columns 11 and 12 list redshifts for the optical counterparts and their origins (see §2.4). Column 13 lists alternative designations for the objects derived from NED.

Table 1. PMN/FSC Sample

FSC Name	PMN Name	Position ^a		Ref.	$S_\nu(25 \mu\text{m})$	$S_\nu(60 \mu\text{m})$	$S_\nu(8 \text{ GHz})$	$S_\nu(5 \text{ GHz})$	Ref.	z	Ref.	Identification
(1)	(2)	RA (J2000)	DEC	(5)	(Jy)	(Jy)	(mJy)	(mJy)	(10)	(11)	(12)	(13)
		(3)	(4)		(6)	(7)	(8)	(9)				
F00123-2356	PMNJ0014-2339	00 14 52.7	-23 39 20	NVSS	<0.085	0.225	20.0	53.8	ATCA	0.0830	R150	Abell 14
F00124-3929 ^b	PMNJ0014-3912	00 14 58.5	-39 12 29	CAB	6.250	77.000	...	112.0	CAB	0.0005	NED	NGC 55
F00183-7111 ^c	PMNJ0020-7055	00 20 34.7	-70 55 26	ATCA	0.133	1.195	51.9	108.6	ATCA	0.3270	DBS	IRAS 00182-7112
F00402-2349	PMNJ0042-2333	00 42 45.8	-23 33 41	NVSS	1.077	10.040	...	56.0	PMN	0.0202	NED	NGC 232
F00450-2533 ^b	PMNJ0047-2517	00 47 33.0	-25 17 18	CAB	155.650	998.730	...	2980.0	CAB	0.0007	NED	NGC 253
F00573-0750	PMNJ0059-0734	00 59 50.3	-07 34 44	NVSS	0.647	8.347	...	44.0	PMN	0.0055	NED	NGC 337
F01009-3241	PMNJ0103-3225	01 03 16.7	-32 25 56	CAB	<0.123	0.291	36.8	95.3	ATCA	0.2560	DBS	PKS 0100-326
F01044-4050	PMNJ0106-4034	01 06 45.1	-40 34 20	ATCA	0.155	0.405	4414.0	3377.0	ATCA	0.5840	NED	Q0104-408
F01053-1746	PMNJ0107-1730	01 07 47.1	-17 30 27	CAB	3.574	22.580	...	83.0	CAB	0.0202	NED	IC 1623
F01219+0331 ^d	PMNJ0124+0348	01 24 34.9	+03 47 29	CAB	3.040	31.550	...	76.0	CAB	0.0076	NED	NGC 520
F01264-5705 ^e	PMNJ0128-5649	01 28 20.5	-56 49 40	ATCA	0.152	0.217	199.3	121.0	ATCA	0.0660	R300	...
F01319-2940	PMNJ0134-2925	01 34 18.1	-29 25 06	CAB	2.447	22.010	...	85.0	CAB	0.0054	NED	NGC 613
F01475-0740	PMNJ0150-0725	01 50 02.6	-07 25 49	CAB	<0.959	1.048	...	205.0	CAB	0.0180	NED	IRAS 01475-0740
F01477-1655 ^f	PMNJ0150-1640	01 50 06.2	-16 40 34	CAB	0.287	0.275	38.6	49.6	ATCA	0.1616	NED	PKS B0147-169
F02207-2127	PMNJ0223-2113	02 23 04.2	-21 14 00	NVSS	1.414	14.770	...	81.0	PMN	0.0050	NED	NGC 908
F02367+0052	PMNJ0239+0106	02 39 23.5	+01 05 38	CAB	<0.212	0.217	...	44.0	CAB	0.0090	NED	NGC 1032
F02386-0828	PMNJ0241-0815	02 41 04.7	-08 15 21	CAB	0.491	0.903	...	2480.0	CAB	0.0052	CAB	NGC 1052
F02391+0013 ^d	PMNJ0241+0026	02 41 45.0	+00 26 37	CAB	2.890	23.270	...	74.0	CAB	0.0037	NED	NGC 1055
F02401-0013 ^d	PMNJ0242-0000	02 42 40.7	-00 00 47	CAB	84.250	181.950	...	1760.0	CAB	0.0037	NED	M77, NGC 1068
F02419-5625	PMNJ0243-5612	02 43 26.5	-56 12 43	ATCA	0.075	0.314	136.3	180.1	ATCA	0.0630	R300	...
F02435-0747 ^d	PMNJ0245-0735	02 45 59.8	-07 34 43	CAB	3.190	29.300	...	103.0	CAB	0.0049	NED	NGC 1084
F02441-3029 ^b	PMNJ0246-3016	02 46 18.9	-30 16 27	CAB	7.700	46.730	...	130.0	CAB	0.0043	NED	NGC 1097
F02470-3130	PMNJ0249-3117	02 49 07.3	-31 17 28	NVSS	<0.062	0.199	24.4	26.2	ATCA	0.0201	NED	IC 1858
F02483-5456	PMNJ0249-5443	02 49 48.2	-54 43 57	ATCA	<0.078	0.170	61.1	107.5	ATCA	0.3940	DBS	...
F03079-3031	PMNJ0310-3019	03 10 01.3	-30 19 37	DSS	0.187	0.242	...	470.0	CAB	0.0680	NED	PKS B0307-305
F03088-0906	PMNJ0311-0855	03 11 17.1	-08 55 08	NVSS	0.447	3.557	...	67.0	PMN	0.0135	NED	Arp 304
F03265-2852	PMNJ0328-2841	03 28 36.4	-28 41 52	CAB	0.244	0.465	254.4	438.6	ATCA	0.1080	NED	PKS B0326-288
F03316-3618 ^b	PMNJ0333-3608	03 33 36.4	-36 08 22	CAB	13.070	84.200	...	210.0	CAB	0.0050	NED	NGC 1365
F03353-2439	PMNJ0337-2430	03 37 28.6	-24 30 03	NVSS	1.502	15.870	...	78.0	PMN	0.0050	NED	NGC 1385
F03384-2129	PMNJ0340-2119	03 40 35.6	-21 19 31	CAB	<0.140	0.235	812.1	828.9	ATCA	0.0480	NED	PKS B0338-214
F03428-4448	PMNJ0344-4438	03 44 35.1	-44 38 31	PMN	0.795	8.579	...	53.0	PMN	0.0039	NED	NGC 1448
F03524-2038 ^d	PMNJ0354-2030	03 54 38.9	-20 30 08	CAB	4.730	35.330	...	102.0	CAB	0.0060	NED	NGC 1482
F03594-6746	PMNJ0359-6738	03 59 38.7	-67 38 01	PMN	2.283	23.670	...	75.0	PMN	0.0044	NED	NGC 1511
F04023-1638	PMNJ0404-1631	04 04 40.5	-16 30 14	NVSS	<0.129	0.300	0.7	5.3	ATCA	0.0270	R150	...
F04137-1144	PMNJ0416-1136	04 16 02.8	-11 36 38	NVSS	<0.166	0.529	39.8	72.4	ATCA	0.0900	R150	IRAS 04136-1144
F04170-6254	PMNJ0417-6246	04 17 38.1	-62 46 58	PMN	1.799	21.530	...	123.0	PMN	0.0043	NED	NGC 1559
F04188-5503	PMNJ0419-5455	04 19 59.0	-54 55 23	PMN	1.219	14.710	...	100.0	PMN	0.0050	NED	NGC 1566
F04207-0127	PMNJ0423-0120	04 23 15.8	-01 20 32	NVSS	0.175	0.446	...	3700.0	CAB	0.9150	NED	PKS 0420-014
F04305+0514	PMNJ0433+0521	04 33 11.0	+05 21 16	CAB	0.635	1.283	...	3486.0	CAB	0.0327	NED	3C 120
F04315-0840	PMNJ0434-0834	04 34 00.0	-08 34 45	NVSS	7.286	32.310	...	63.0	PMN	0.0159	NED	NGC 1614
F04367-2726	PMNJ0438-2720	04 38 46.3	-27 20 54	NVSS	<0.082	0.585	27.1	45.0	ATCA	0.1110	DBS	IRAS 04367-2726

Table 1—Continued

FSC Name	PMN Name	Position ^a		Ref.	$S_{\nu}(25 \mu\text{m})$ (Jy)	$S_{\nu}(60 \mu\text{m})$ (Jy)	$S_{\nu}(8 \text{ GHz})$ (mJy)	$S_{\nu}(5 \text{ GHz})$ (mJy)	Ref.	z	Ref.	Identification
		RA (J2000)	DEC									
(1)	(2)	(3)	(4)	(5)	(6)	(7)	(8)	(9)	(10)	(11)	(12)	(13)
F04449-5920	PMNJ0445-5914	04 45 43.1	-59 14 47	PMN	4.034	32.960	...	114.0	PMN	0.0045	NED	NGC 1672
F04461-0624	PMNJ0448-0618	04 48 37.1	-06 19 13	NVSS	0.667	5.952	...	45.0	PMN	0.0152	NED	NGC 1667
F04500-0311	PMNJ0452-0306	04 52 31.3	-03 06 22	NVSS	<0.113	0.776	...	103.0	CAB	0.0150	NED	NGC 1684
F05059-3734	PMNJ0507-3731	05 07 42.2	-37 30 49	CAB	16.140	87.810	...	154.0	CAB	0.0027	NED	NGC 1808
F05212-3630	PMNJ0522-3628	05 22 57.9	-36 27 32	CAB	0.158	0.307	3836.0	5740.0	ATCA	0.0553	NED	Q0521-365
F05246+0103	PMNJ0527+0105	05 27 16.0	+01 06 01	CAB	0.544	2.474	...	177.0	CAB	0.0969	NED	IRAS 05246+0103
F05265-4720	PMNJ0527-4718	05 27 55.9	-47 18 28	ATCA	0.074	0.902	141.4	48.0	ATCA	0.1340	DBS	IRAS 05265-4720
F05312-2158	PMNJ0533-2156	05 33 21.6	-21 56 45	NVSS	0.722	7.976	...	55.0	PMN	0.0055	NED	NGC 1964
F05373-4406	PMNJ0538-4405	05 38 50.4	-44 05 09	ATCA	0.220	0.418	2388.0	2286.0	ATCA	0.8940	NED	PKS 0537-441
F05497-0728	PMNJ0552-0727	05 52 11.2	-07 27 24	CAB	0.840	4.129	...	163.0	CAB	0.0076	NED	NGC 2110
F05585-5026	PMNJ0559-5027	05 59 47.4	-50 26 52	ATCA	0.081	0.210	73.5	85.2	ATCA	0.1370	NED	Q0558-504
F06035-7102	PMNJ0602-7102	06 02 46.4	-71 02 48	PMN	0.574	5.127	...	51.0	PMN	0.0795	NED	IRAS 06035-7102
F06065-7934	PMNJ0603-7934	06 03 06.0	-79 34 51	ATCA	<0.068	0.329	268.0	508.6	ATCA	0.2870	DBS	PKS 0606-796
F06090-1922	PMNJ0611-1923	06 11 17.3	-19 23 00	ATCA	0.210	0.136	6.9	9.4	ATCA	0.1340	R150	...
F06142-2121	PMNJ0616-2122	06 16 22.8	-21 22 21	PMN	1.548	14.550	...	94.0	CAB	0.0086	NED	IC 2163
F06185-0828	PMNJ0620-0829	06 20 56.4	-08 29 41	NVSS	1.129	14.050	...	81.0	PMN	0.0025	NED	UGCA 127
F06195-4503	PMNJ0620-4504	06 21 01.3	-45 04 40	ATCA	0.060	0.281	382.3	493.9	ATCA	0.2060	DBS	PKS B0619-450
F06218-8636	PMNJ0605-8637	06 05 25.7	-86 37 44	PMN	0.708	6.883	...	30.0	PMN	0.0060	NED	ESO 005-G004
F06374-7513	PMNJ0635-7516	06 35 46.5	-75 16 17	ATCA	0.107	0.178	5458.0	6365.0	ATCA	0.6540	NED	Q0637-752
F07160-6215	PMNJ0716-6221	07 16 38.1	-62 21 17	PMN	2.205	19.310	...	35.0	PMN	0.0108	NED	NGC 2369
F07365-6924	PMNJ0736-6931	07 36 21.8	-69 31 44	PMN	0.452	8.145	...	105.0	PMN	0.0048	NED	NGC 2442
F07543+1004	PMNJ0757+0956	07 57 06.6	+09 56 35	CAB	0.235	0.206	...	771.0	CAB	0.6600	NED	PKS 0754+100
F08014+0515	PMNJ0804+0507	08 04 05.8	+05 06 49	CAB	2.075	1.892	...	56.0	CAB	0.0135	NED	UGC 04203
F08064-1018	PMNJ0808-1027	08 08 53.6	-10 27 40	CAB	0.337	0.534	1070.0	1732.0	ATCA	0.1100	NED	3C 195
F08291+0439	PMNJ0831+0429	08 31 48.8	+04 29 39	CAB	0.256	0.428	...	2136.0	CAB	0.1800	NED	Q0829+046
F08311-2248	PMNJ0833-2259	08 33 22.6	-22 59 06	PMN	0.843	6.312	...	42.0	PMN	0.0056	NED	NGC 2613
F09165-0726	PMNJ0919-0739	09 19 01.8	-07 39 07	CAB	<0.074	0.267	...	156.0	CAB	0.2730	DBS	...
F09253-3412	PMNJ0927-3424	09 27 24.4	-34 24 57	ATCA	0.189	0.388	18.3	37.7	ATCA	0.1780	DBS	...
F09323+0732	PMNJ0935+0719	09 35 01.0	+07 19 17	CAB	<0.147	0.260	...	353.0	CAB	0.2900	R150	OK+052
F09416-0137	PMNJ0944-0151	09 44 09.9	-01 51 15	NVSS	<0.174	1.172	...	70.0	PMN	0.1120	DBS	IRAS 09415-0137
F09426-1928	PMNJ0944-1942	09 44 59.8	-19 42 44	NVSS	0.994	3.909	24.5	42.9	ATCA	0.0325	NED	ESO 566-IG008
F09496-7341	PMNJ0950-7355	09 50 09.2	-73 55 05	PMN	1.031	10.600	...	38.0	PMN	0.0042	NED	NGC 3059
F10015-0614	PMNJ1004-0628	10 04 02.0	-06 28 32	NVSS	1.043	10.700	...	41.0	PMN	0.0168	NED	NGC 3110
F10116+0342 ^d	PMNJ1014+0327	10 14 15.1	+03 27 57	CAB	0.920	8.060	...	46.0	CAB	0.0033	NED	NGC 3169
F10227-8251	PMNJ1021-8306	10 21 34.8	-83 06 49	ATCA	0.252	0.366	14.9	31.4	ATCA	0.0860	DBS	IRAS 10227-8251
F10257-4339	PMNJ1027-4354	10 27 51.6	-43 54 18	PMN	16.030	88.300	...	319.0	PMN	0.0091	NED	NGC 3256
F10459-2453	PMNJ1048-2510	10 48 23.6	-25 09 44	NVSS	0.753	2.251	16.3	21.2	ATCA	0.0137	NED	NGC 3393
F10560-0219	PMNJ1058-0236	10 58 35.4	-02 35 52	NVSS	<0.192	1.304	...	46.0	PMN	0.0360	NED	IRAS 10560-0219
F11032+0014 ^b	PMNJ1105-0002	11 05 48.5	-00 02 06	PMN	4.360	44.020	...	170.0	PMN	0.0027	NED	NGC 3521
F11143-7556	PMNJ1115-7613	11 15 56.1	-76 13 20	PMN	4.240	42.800	...	120.0	PMN	0.0056	NED	NGC 3620
F11158-3232 ^b	PMNJ1118-3248	11 18 17.4	-32 48 51	PMN	5.090	29.620	...	80.0	CAB	0.0024	NED	NGC 3621

Table 1—Continued

FSC Name	PMN Name	Position ^a		Ref.	$S_\nu(25 \mu\text{m})$	$S_\nu(60 \mu\text{m})$	$S_\nu(8 \text{ GHz})$	$S_\nu(5 \text{ GHz})$	Ref.	z	Ref.	Identification
		RA (J2000)	DEC		(Jy)	(Jy)	(mJy)	(mJy)				
(1)	(2)	(3)	(4)	(5)	(6)	(7)	(8)	(9)	(10)	(11)	(12)	(13)
F11243-2244	PMNJ1126-2300	11 26 53.6	-23 01 14	ATCA	0.115	0.299	35.2	64.2	ATCA	0.1710	DBS	...
F11334-3743	PMNJ1135-3800	11 35 53.3	-37 59 52	NVSS	0.302	4.410	...	59.0	PMN	0.0091	NED	NGC 3749
F11445-3755	PMNJ1147-3812	11 47 01.3	-38 12 11	CAB	0.151	0.291	2514.0	2014.0	ATCA	1.0480	NED	PKS 1144-379
F11506-3851	PMNJ1153-3907	11 53 11.8	-39 07 48	NVSS	2.324	32.680	...	56.0	PMN	0.0108	NED	ESO 320-G030
F11593-1836 ^d	PMNJ1201-1852	12 01 54.9	-18 52 46	NVSS	6.580	48.680	...	197.0	CAB	0.0055	NED	Arp 244
F12173-3541	PMNJ1219-3557	12 19 58.9	-35 57 38	CAB	0.168	2.248	65.3	119.0	ATCA	0.0572	NED	ESO 380-IG015
F12183-1015	PMNJ1220-1032	12 20 53.7	-10 32 27	ATCA	<0.294	0.246	45.7	55.8	ATCA	0.3000	DBS	...
F12193+0445 ^d	PMNJ1221+0428	12 21 55.0	+04 28 24	CAB	4.900	37.530	...	157.0	CAB	0.0052	NED	M61, NGC 4303
F12193-4303	PMNJ1222-4320	12 22 00.7	-43 20 35	PMN	0.524	4.704	...	57.0	PMN	0.0235	NED	ESO 267-IG041
F12265+0219	PMNJ1229+0203	12 29 06.7	+02 03 08	CAB	0.896	2.060	...	43600.0	CAB	0.1583	NED	3C 273
F12315+0255 ^d	PMNJ1234+0238	12 34 08.3	+02 39 14	CAB	3.530	33.160	...	110.0	PMN	0.0058	NED	NGC 4527
F12319+0227	PMNJ1234+0211	12 34 27.0	+02 11 17	CAB	3.574	30.130	...	114.0	PMN	0.0060	NED	NGC 4536
F12374-1120	PMNJ1239-1137	12 39 59.4	-11 37 24	CAB	0.497	3.113	107.0	103.9	ATCA	0.0028	CAB	M104, NGC 4594
F12425-0011 ^d	PMNJ1245-0027	12 45 08.4	-00 27 46	CAB	3.680	37.340	...	210.0	CAB	0.0051	NED	NGC 4666
F12440-2531	PMNJ1246-2547	12 46 46.7	-25 47 50	CAB	0.163	0.408	1343.0	1195.0	ATCA	0.6380	NED	Q1244-255
F12535-0530	PMNJ1256-0547	12 56 11.1	-05 47 22	CAB	<0.213	0.253	...	10500.0	CAB	0.5380	NED	3C 279
F12552-4559	PMNJ1258-4615	12 58 06.1	-46 15 55	PMN	1.377	16.160	...	61.0	PMN	0.0073	NED	NGC 4835
F13025-4912	PMNJ1305-4928	13 05 27.1	-49 28 09	PMN	14.450	359.300	...	3055.0	PMN	0.0019	NED	NGC 4945
F13059-2406	PMNJ1308-2422	13 08 42.0	-24 22 58	CAB	0.671	1.440	129.7	222.0	ATCA	0.0139	NED	IRAS 13059-2407
F13170-2708	PMNJ1319-2724	13 19 50.0	-27 24 37	CAB	0.715	9.967	152.8	149.2	ATCA	0.0073	CAB	NGC 5078
F13174-1651	PMNJ1320-1706	13 20 06.2	-17 07 06	NVSS	<0.187	0.408	26.4	33.7	ATCA	0.0210	NED	VV 802
F13197-1627	PMNJ1322-1643	13 22 24.4	-16 43 44	CAB	2.855	5.895	54.9	103.6	ATCA	0.0165	NED	MCG-03-34-063
F13229-2934	PMNJ1325-2949	13 25 44.0	-29 50 01	NVSS	2.401	16.910	...	107.0	PMN	0.0137	NED	NGC 5135
F13334-0814	PMNJ1336-0830	13 36 08.1	-08 29 52	CAB	0.239	0.732	...	650.0	CAB	0.0231	NED	NGC 5232
F13341-2936 ^b	PMNJ1336-2951	13 37 00.3	-29 51 56	CAB	47.720	266.030	...	770.0	CAB	0.0017	NED	M83, NGC 5236
F13353-1737	PMNJ1338-1753	13 38 03.3	-17 53 00	NVSS	0.452	8.072	...	61.0	PMN	0.0045	NED	NGC 5247
F13370-3123	PMNJ1339-3138	13 39 55.9	-31 38 28	NVSS	11.960	30.510	...	90.0	PMN	0.0014	NED	NGC 5253
F13478-4848	PMNJ1350-4903	13 50 54.1	-49 03 31	PMN	1.697	13.040	...	46.0	PMN	0.0103	NED	ESO 221-IG010
F13536+0529	PMNJ1356+0515	13 56 07.1	+05 15 17	CAB	<0.240	1.693	...	121.0	CAB	0.0034	CAB	NGC 5363
F14111+0753	PMNJ1413+0739	14 13 38.8	+07 39 34	NVSS	0.235	1.308	...	49.0	CAB	0.0235	NED	NGC 5514
F14165+0642	PMNJ1419+0628	14 19 08.2	+06 28 33	CAB	<0.241	0.218	...	1530.0	CAB	1.4360	NED	3C 298
F14294-4357	PMNJ1432-4411	14 32 37.5	-44 11 02	PMN	3.647	19.490	...	87.0	PMN	0.0040	NED	NGC 5643
F14376-0004	PMNJ1440-0017	14 40 11.3	-00 17 26	NVSS	2.583	19.820	...	81.0	PMN	0.0063	NED	NGC 5713
F14381-3901	PMNJ1441-3913	14 41 15.1	-39 13 48	ATCA	0.310	0.360	130.3	174.4	ATCA	0.1380	DBS	...
F14501+0639	PMNJ1452+0627	14 52 39.3	+06 27 37	CAB	<0.142	0.292	...	224.0	CAB	0.2670	DBS	...
F14565-1629 ^d	PMNJ1459-1641	14 59 24.7	-16 41 41	CAB	0.450	6.360	244.1	470.5	ATCA	0.0116	CAB	NGC 5793
F15066-7240	PMNJ1511-7251	15 11 44.2	-72 51 01	PMN	0.760	7.189	...	28.0	PMN	0.0102	NED	NGC 5833
F15129+0432	PMNJ1515+0421	15 15 25.0	+04 21 46	CAB	<0.117	0.775	...	69.0	CAB	0.0951	NED	IRAS 15129+0432
F15306-0832	PMNJ1533-0842	15 33 20.7	-08 42 03	NVSS	0.357	1.944	...	103.0	PMN	0.0230	NED	MCG-01-40-001
F15366+0544	PMNJ1539+0534	15 39 05.1	+05 34 38	NVSS	<0.129	0.360	...	217.0	PMN	0.0260	NED	MCG+01-40-010
F15494-7905	PMNJ1556-7914	15 56 58.9	-79 14 04	ATCA	0.471	1.015	2400.0	3680.0	ATCA	0.1500	NED	PKS 1549-79

Table 1—Continued

FSC Name	PMN Name	Position ^a		Ref.	$S_\nu(25 \mu\text{m})$ (Jy)	$S_\nu(60 \mu\text{m})$ (Jy)	$S_\nu(8 \text{ GHz})$ (mJy)	$S_\nu(5 \text{ GHz})$ (mJy)	Ref.	z	Ref.	Identification
		RA (J2000)	DEC									
(1)	(2)	(3)	(4)	(5)	(6)	(7)	(8)	(9)	(10)	(11)	(12)	(13)
F15599+0206	PMNJ1602+0157	16 02 27.4	+01 57 56	NED	0.319	0.599	...	2800.0	CAB	0.1040	NED	3C 327
F16154-7001	PMNJ1620-7008	16 20 36.1	-70 08 50	PMN	0.680	6.848	...	35.0	PMN	0.0114	NED	IC 4595
F16159-0402	PMNJ1618-0410	16 18 36.4	-04 09 43	NVSS	0.299	0.979	...	66.0	PMN	0.2126	NED	IRAS 16159-0402
F16164-0746	PMNJ1619-0753	16 19 11.8	-07 54 03	NVSS	0.562	10.180	...	41.0	PMN	0.0271	NED	IRAS 16164-0746
F16254-6735	PMNJ1630-6742	16 30 28.9	-67 42 21	ATCA	0.114	0.784	17.0	26.5	ATCA	0.0404	NED	IRAS 16254-6735
F16431+0217	PMNJ1645+0211	16 45 42.3	+02 11 45	CAB	<0.176	0.248	...	654.0	CAB	0.0960	DBS	4C +02.42
F16504+0228	PMNJ1653+0224	16 52 58.7	+02 24 04	CAB	3.417	22.680	...	179.0	CAB	0.0245	NED	NGC 6240
F17123-6245	PMNJ1716-6249	17 16 54.0	-62 49 10	PMN	2.272	14.650	...	39.0	PMN	0.0037	NED	NGC 6300
F17182-7353	PMNJ1724-7356	17 24 31.2	-73 56 14	PMN	0.272	3.582	...	21.0	PMN	0.0160	NED	IC 4644
F17207-0014	PMNJ1723-0016	17 23 22.0	-00 17 02	NVSS	1.658	31.140	...	66.0	PMN	0.0428	NED	IRAS 17208-0014
F18093-5744	PMNJ1813-5743	18 13 42.6	-57 43 45	PMN	2.375	15.190	...	60.0	PMN	0.0173	NED	IC 4687
F18293-3413	PMNJ1832-3411	18 32 41.2	-34 11 28	PMN	3.759	34.190	...	144.0	PMN	0.0180	NED	IRAS 18293-3413
F18325-5926	PMNJ1836-5924	18 36 58.2	-59 24 08	ATCA	1.385	3.227	36.3	66.1	ATCA	0.0192	NED	Fairall 90
F19071-5707	PMNJ1911-5702	19 11 18.0	-57 02 38	PMN	0.724	9.425	...	35.0	PMN	0.0104	NED	NGC 6753
F19254-7245	PMNJ1931-7239	19 31 21.4	-72 39 21	ATCA	1.242	5.484	56.8	94.4	ATCA	0.0617	NED	Superantennae
F19384-7045	PMNJ1943-7038	19 43 48.1	-70 38 22	PMN	0.858	6.865	...	32.0	PMN	0.0116	NED	NGC 6808
F19393-5846	PMNJ1943-5840	19 43 32.2	-58 40 16	PMN	3.491	17.790	...	72.0	PMN	0.0068	NED	NGC 6810
F19497+0222	PMNJ1952+0230	19 52 13.1	+02 30 26	NVSS	0.452	0.452	...	2370.0	CAB	0.0590	NED	3C 403
F19542-3804	PMNJ1957-3755	19 57 37.5	-37 56 09	NVSS	1.171	6.050	...	90.0	PMN	0.0190	NED	ESO 339-G011
F20057-4858	PMNJ2009-4849	20 09 25.4	-48 49 54	ATCA	0.235	0.240	1030.0	1111.0	ATCA	0.0710	NED	Q2005-489
F20203-5733	PMNJ2024-5723	20 24 20.5	-57 23 43	ATCA	0.193	0.273	387.9	760.1	ATCA	0.3520	NED	PKS 2020-57
F20221-2458	PMNJ2025-2448	20 25 07.1	-24 48 33	NVSS	1.343	13.160	...	64.0	PMN	0.0105	NED	NGC 6907
F20304-0211	PMNJ2033-0201	20 33 08.2	-02 01 20	PMN	0.512	5.586	...	48.0	PMN	0.0199	NED	NGC 6926
F20482-5715	PMNJ2051-5704	20 52 02.1	-57 04 07	ATCA	3.910	5.337	197.7	368.0	ATCA	0.0110	NED	IC 5063
F20517-5809	PMNJ2055-5758	20 55 34.7	-57 58 10	ATCA	<0.060	0.351	30.2	45.2	ATCA	0.1930	DBS	...
F21139-6613	PMNJ2118-6600	21 18 14.5	-66 00 17	ATCA	<0.078	0.318	10.2	21.0	ATCA	0.1530	DBS	...
F21309-0726	PMNJ2133-0712	21 33 33.3	-07 12 51	ATCA	0.190	0.330	34.7	62.4	ATCA	0.0870	DBS	...
F21356-1015	PMNJ2138-1001	21 38 19.9	-10 01 53	ATCA	0.159	0.460	27.0	46.5	ATCA	0.2060	DBS	IRAS 21356-1015
F21497-0824	PMNJ2152-0810	21 52 26.1	-08 10 24	NVSS	0.635	3.124	...	65.0	PMN	0.0345	NED	IRAS 21497-0824
F21511-4606	PMNJ2154-4553	21 54 22.9	-45 52 31	ATCA	<0.103	0.190	34.8	41.1	ATCA	0.1460	DBS	...
F21527-2856	PMNJ2155-2841	21 55 38.1	-28 42 07	ATCA	<0.161	0.230	90.5	144.3	ATCA	0.2320	DBS	...
F21529-6955	PMNJ2157-6941	21 57 06.0	-69 41 23	ATCA	0.124	0.185	...	11649.0	PMN	0.0283	NED	PKS 2153-69
F21583-3800	PMNJ2201-3746	22 01 17.6	-37 46 28	NVSS	0.141	0.349	...	644.0	PMN	0.0330	NED	PKS 2158-380
F22061-4724	PMNJ2209-4710	22 09 16.2	-47 10 00	ATCA	0.742	2.666	140.2	153.0	ATCA	0.0060	NED	NGC 7213
F22073-4044	PMNJ2210-4029	22 10 18.6	-40 29 54	ATCA	<0.117	0.225	117.1	198.6	ATCA	PKS B2207-407
F22132-3705	PMNJ2216-3651	22 16 09.0	-36 50 40	NVSS	2.219	18.980	...	79.0	PMN	0.0114	NED	IC 5179
F22231-0512	PMNJ2225-0457	22 25 47.3	-04 57 02	NVSS	0.284	0.597	...	6382.0	PMN	1.4040	NED	3C 446
F22521-3929	PMNJ2254-3913	22 54 59.9	-39 13 01	ATCA	0.135	0.283	174.7	304.5	ATCA	0.2587	DBS	PKS 2252-394
F22537-6512	PMNJ2256-6456	22 56 57.9	-64 56 03	ATCA	0.199	1.247	113.0	194.5	ATCA	0.1200	NED	PKS 2253-652
F22544-3643	PMNJ2257-3627	22 57 10.7	-36 27 43	NVSS	<0.210	0.467	1023.0	1263.0	ATCA	0.0056	NED	IC 1459
F23002-5828	PMNJ2303-5812	23 03 18.3	-58 12 35	ATCA	0.121	0.282	13.0	21.6	ATCA	0.2100	DBS	...

Table 1—Continued

FSC Name	PMN Name	Position ^a		Ref.	$S_\nu(25 \mu\text{m})$ (Jy)	$S_\nu(60 \mu\text{m})$ (Jy)	$S_\nu(8 \text{ GHz})$ (mJy)	$S_\nu(5 \text{ GHz})$ (mJy)	Ref.	z	Ref.	Identification
		RA (J2000)	DEC									
(1)	(2)	(3)	(4)	(5)	(6)	(7)	(8)	(9)	(10)	(11)	(12)	(13)
F23007+0836 ^d	PMNJ2303+0852	23 03 15.5	+08 52 26	CAB	5.840	27.680	...	61.0	CAB	0.0163	NED	NGC 7469
F23075-5957	PMNJ2310-5941	23 10 28.5	-59 41 11	ATCA	<0.090	0.713	176.7	154.3	ATCA	0.1410	DBS	IRAS 23075-5957
F23121+0415 ^d	PMNJ2314+0431	23 14 44.0	+04 32 02	CAB	1.990	20.590	...	48.0	CAB	0.0089	NED	NGC 7541
F23133-4251	PMNJ2316-4234	23 16 08.0	-42 34 52	PMN	12.160	72.030	...	139.0	PMN	0.0053	NED	NGC 7552
F23135-4745	PMNJ2316-4729	23 16 27.0	-47 29 24	ATCA	<0.084	0.231	215.2	366.3	ATCA	0.6770	NED	PKS 2313-477
F23140+0348	PMNJ2316+0405	23 16 35.2	+04 05 18	CAB	<0.185	0.602	...	1348.0	CAB	0.2199	NED	3C 459
F23156-4238	PMNJ2318-4221	23 18 22.7	-42 21 40	PMN	6.436	49.100	...	143.0	PMN	0.0052	NED	NGC 7582
F23254+0830	PMNJ2327+0846	23 27 56.6	+08 46 45	CAB	1.896	5.588	...	67.0	CAB	0.0290	NED	NGC 7674
F23389+0300	PMNJ2341+0317	23 41 30.3	+03 17 27	CAB	<0.349	1.233	...	196.0	CAB	0.1450	NED	PKS 2338+03
F23389-6139	PMNJ2341-6122	23 41 43.6	-61 22 53	ATCA	0.244	3.628	34.7	57.1	ATCA	0.0927	NED	IRAS 23389-6139
F23400-8705	PMNJ2344-8648	23 44 16.2	-86 48 32	ATCA	0.064	0.221	54.0	104.7	ATCA	0.1060	DBS	PKS 2340-870
F23475-7407	PMNJ2350-7350	23 50 12.1	-73 50 32	ATCA	<0.071	0.177	12.6	14.6	ATCA	0.1050	DBS	...
F23493-0126	PMNJ2351-0109	23 51 56.2	-01 09 16	NVSS	<0.230	0.241	...	689.0	PMN	0.1740	NED	Q2349-014
F23565-7631	PMNJ2359-7614	23 59 06.5	-76 14 49	ATCA	<0.053	0.353	19.3	26.0	ATCA	0.0820	DBS	...

^aRight Ascension is given in units hours, minutes and seconds. Declination is given in units of degrees, arcminutes and arcseconds.

^bFIR fluxes are from Rice et al. (1988).

^cRadio/FIR association discussed by Norris et al. (1988).

^dFIR fluxes are from Soifer et al. (1989).

^eVaried by factor of 1.85 at 8.6 GHz between July 1996 (107.7 mJy) and Jan/Feb 1998 (199.3 mJy).

^fATCA flux is fainter than CAB ($S_\nu(4.8\text{GHz}) = 188 \text{ mJy}$) and PMN ($S_\nu(4.8\text{GHz}) = 172.0 \text{ mJy}$).

2.3. Reliability of Identifications

A sample selected by positional coincidence alone may contain spurious associations due to the chance presence of a PMN source within the *IRAS* 3σ error ellipse. We have estimated the number of chance coincidences in our sample from both the average PMN source density and by offsetting the positions and recalculating the cross-correlation.

The number of chance coincidences can be estimated from the product of the average PMN source density in the overlap area between the PMN and FSC surveys and the total sky area contained within all *IRAS* 3σ error ellipses. The survey overlap area is 6.13 steradians, which is bounded by declination $+10^\circ$ and -87.5° and excludes the Galactic plane in the region $|b| < 10^\circ$ and a further area of 1.8×10^{-2} steradians due to the Large and Small Magellanic Clouds. The PMN catalog contains 38,170 sources within this survey overlap area, corresponding to an average PMN source density of $6.2 \times 10^3 \text{ sr}^{-1}$. A total sky area of 3.85×10^{-3} steradians is contained within the 3σ error ellipses of all candidate $60 \mu\text{m}$ *IRAS* FSC sources searched. This includes the 3σ error ellipses of both the FSC $60 \mu\text{m}$ sources with radio counterparts and those without counterparts. We therefore expect 23.9 chance coincidences of PMN sources within unrelated FSC error ellipses.

A more accurate method is to offset the PMN source positions and to recalculate the correlations. Offsetting the PMN positions further than the extent of the largest *IRAS* error ellipse ensures that all derived correlations are spurious. Offsetting by an amount not much larger than this ensures that the correlations are recalculated with close to the true PMN source density in the vicinity of each FSC source. We chose to offset the PMN positions 2 arcmin north. A total of 25 spurious correlations were then obtained. We are therefore confident that the number of chance coincidences included in our full sample is ~ 24 -25.

The full sample contains 243 valid PMN/FSC correlations comprising 178 extragalactic objects with optical counterparts, 24 extragalactic correlations that were rejected on the basis of optical confusion, and 41 Galactic objects. In all, 17% of the valid correlations are identified with Galactic objects. The same percentage of Galactic objects should be present among the ~ 24 -25 expected chance coincidences, so our extragalactic correlations alone should include ~ 21 chance coincidences. This is consistent with the 24 extragalactic correlations that in fact were rejected on the basis of optical confusion.

Consequently, we are confident that the final list of 178 PMN/FSC identifications are reliable and that chance coincidences in our sample have been identified and excluded by reference to the optical images.

2.4. Redshifts

Redshifts for the optical counterparts of 143 of the PMN/FSC objects are available in the NED database. Redshifts for some other objects have been derived from the proper distances tabulated from various sources by CAB.

Redshifts for most of the remaining objects were derived from optical spectra obtained with the Double Beam Spectrograph (Rodgers, Conroy, & Bloxham 1988, DBS) on the Australian National University (ANU) 2.3 m telescope at Siding Spring Observatory. The B300 and R316 gratings were used in the blue and red arms, respectively, with a $2''$ slit giving full wavelength coverage from $\sim 3500 \text{ \AA}$ to $\sim 9000 \text{ \AA}$ with a resolution of $\sim 4 \text{ \AA}$. Two dichroic mirrors were used for different redshift regimes to avoid locating prominent emission lines near the cutoff wavelength; dichroic #3 has a cut-off wavelength of 6200 \AA so was used for $z < 0.20$ and $z > 0.32$, and dichroic #1 has a cutoff wavelength of 5630 \AA so was used for $0.20 < z < 0.32$. Each observation consisted of three unguided exposures each of 1200 s

duration. Object acquisition was by offsetting from a nearby star before each 1200 s exposure. Telescope tracking was adequate to hold the object within the 2'' slit over this time. The data were reduced using the *onedspec* package within *IRAF*⁹. Generally, a 9'' region around each object was extracted from the two dimensional image. Wavelength calibration was based on a single Fe-Ar arc spectrum obtained each night. Wavelength shifts during each night were tracked using night sky emission lines recorded on each exposure.

Some redshifts were determined using the Nasmyth B Imager (Rodgers, Bloxham, & Conroy 1993) on the ANU 2.3 m telescope. Spectra were measured through either the R150 or R300 grisms with a 2.5'' wide slit. The R150 grism delivered a resolution of $\sim 44 \text{ \AA}$ over a wavelength range of $\sim 4000\text{--}10000 \text{ \AA}$. The R300 grism delivered a resolution of $\sim 22 \text{ \AA}$ over a wavelength range of typically $6000\text{--}9000 \text{ \AA}$. Unguided exposures of 1800 s were obtained, and He and Ar arc spectra were recorded for wavelength calibration. The target acquisition and data reduction procedures were the same as described above for the DBS spectra.

For all object spectra obtained at the 2.3 m telescope, measurements of smooth-spectrum stars obtained at similar airmasses were used to remove terrestrial absorption features. Flux calibration was performed relative to standard stars from either Oke & Gunn (1983) or Hamuy et al. (1992, 1994). Emission-line redshifts were measured using Gaussian line profile fits in *splot*. The redshifts are listed in Table 1.

3. Results

3.1. Radio/Far-infrared Correlations

The radio/FIR flux density diagram for the PMN/FSC sample is shown in Fig. 1(a). The tight sequence of FIR-bright objects is a manifestation of the well-known radio/FIR correlation for radio-quiet objects. Of particular note is the large number of relatively FIR-faint radio-excess objects located above the radio-quiet relation. These objects are also present in the sample of CAB (open symbols in Fig. 1(a)) but were not specifically noted by these authors. Their sample has a similar radio flux density to the PMN/FSC sample and both were selected from the *IRAS* FSC ($60 \mu\text{m}$ flux limit of $\sim 200 \text{ mJy}$), but CAB imposed the additional criterion that $S_\nu(60 \mu\text{m}) > S_\nu(12 \mu\text{m})$. Only a few radio-excess objects are present in other samples with higher FIR flux density limits (e.g., Yun et al. (2001) with a $60 \mu\text{m}$ flux limit of 2 Jy and Corbett et al. (2002) with a $60 \mu\text{m}$ flux limit of 4 Jy). A large number of the radio-excess objects appear at $60 \mu\text{m}$ fluxes below 1 Jy, with many of these having intermediate radio excesses. We refer to these latter objects as radio-intermediate objects. The analysis presented in §2.3 demonstrates the reliability of our sample identifications. The FIR-faint radio-intermediate objects therefore appear to be a new population of extragalactic objects.

It is useful to consider the locations of well-studied objects in the radio/FIR flux density diagram in order to determine what types of objects populate the radio-intermediate region of Fig. 1. The positions of a range of well-studied active and starburst galaxies in the radio/FIR flux density diagram are shown in Fig. 1(b). Table 2 lists the references to these data. The relative densities of these objects in Fig. 1(b) are not indicative of unbiased samples because the objects are drawn from heterogeneous samples with different flux density limits. Nevertheless, Fig. 1(b) is still useful in highlighting where different classes of objects lie. As is well-known, starburst galaxies, Seyfert galaxies, and radio-quiet quasars generally follow

⁹*IRAF (Image Reduction and Analysis Facility)* is distributed by the National Optical Astronomy Observatories, which are operated by the Association of Universities for Research in Astronomy, Inc., under cooperative agreement with the National Science Foundation.

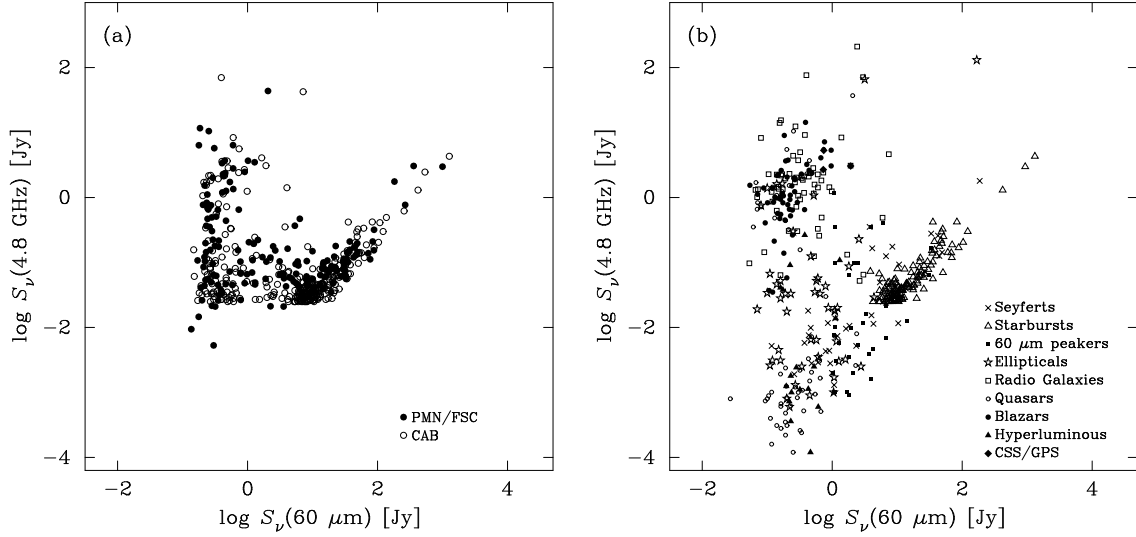


Fig. 1.— (a) Radio/FIR flux density diagram for the PMN/FSC sample (*solid symbols*) and the CAB sample (*open symbols*). (b) Radio/FIR flux density diagram for the starburst and active galaxy samples listed in Table 2.

Table 2. Comparison Objects

Class	Far-Infrared Data	Radio Data
Seyfert galaxies	Edelson, Malkan, & Rieke (1987)	Edelson (1987)
Infrared galaxies	Soifer et al. (1989)	Condon, Frayer, & Broderick (1991b)
...	...	CAB
60 μm Peakers	Vader et al. (1993)	Heisler, Lumsden, & Bailey (1997)
Nearby ellipticals	Knapp et al. (1989)	Sadler (1984)
...	...	Sadler, Jenkins, & Kotanyi (1989)
Radio galaxies	Golombek, Miley, & Neugebauer (1988)	Kuhr et al. (1981)
...	Knapp, Bies, & van Gorkom (1990)	...
Quasars	Sanders et al. (1989)	Kellerman et al. (1989)
...	Elvis et al. (1994)	Elvis et al. (1994)
Blazars	Impey & Neugebauer (1988)	Owen, Spanger, & Cotton (1980)
...	Landau et al. (1986)	Landau et al. (1986)
Hyperluminous galaxies	Rowan-Robinson (2000)	Barvainis & Antonucci (1989); Barvainis & Lonsdale (1997)
...	...	Blundell & Lacy (1995); Gregory & Condon (1991)
...	...	Griffith & Wright (1993); Kellerman et al. (1989)
...	...	Rowan-Robinson (2000)
...	...	Becker et al. (1995); Condon et al. (1998)
...	...	(based on $S_\nu(1.4 \text{ GHz})$ with $\alpha = -0.8$)
CSS and GPS sources	IRAS FSC	O’Dea (1998)

the radio-quiet correlation in Fig. 1, with some Seyfert galaxies lying significantly above the radio-quiet sequence. 3C radio galaxies and radio-loud quasars follow the apparent radio-loud equivalent of this relation. This is a selection effect due to the high 3C flux density limit: The 3C flux limit of ~ 10 Jy at 408 MHz (Bennett 1963) for a steep spectrum object with radio spectral index of 0.7 corresponds to ~ 1.7 Jy at 5 GHz. This is close to the lower edge of the apparent radio-loud clump of objects in Fig. 1(b). Interestingly, many of the nearby elliptical galaxies surveyed for radio emission by Sadler (1984) have radio and FIR flux densities that place them in the radio-intermediate region of Fig. 1(b). Some well-studied radio galaxies, Seyfert galaxies, and $60 \mu\text{m}$ Peakers also extend into this region. These are discussed in more detail in §4.

The corresponding radio/FIR luminosity diagram for the PMN/FSC sample is shown in Fig. 2(a). Distances have been derived from the redshifts listed in Table 1. The CAB objects are also plotted in Fig. 2(a) with distances taken from that paper. Specific luminosity (i.e., L_ν) is plotted for the radio data and monochromatic luminosity (i.e., νL_ν) is plotted for the FIR data. There are two points to note from this figure: First, the radio-excess objects extend over the full range of $60 \mu\text{m}$ luminosities shown by the radio-quiet objects (from $\sim 10^8 L_\odot$ to $\gtrsim 10^{12.5} L_\odot$). The high end is in the range of ultra-luminous infrared galaxies. In fact, the radio-loud objects extend to even higher FIR luminosities than radio-quiet objects. There is possibly a lack of low FIR luminosity radio-excess objects in the PMN/FSC sample. However, this may be due to nearby lobe-dominated radio galaxies being excluded from the PMN/FSC sample due to large position offsets between their radio (lobe) and FIR (host) emission. Second, there is no obvious radio-loud equivalent of the radio-quiet radio/FIR luminosity correlation in these samples. In fact, the radio-excess region appears to be populated uniformly. The distribution of radio-excess objects is accurately represented in Fig. 2(a) at high radio excesses. However, objects with small radio excesses are under-represented in Fig. 2(a) because objects are missing that fall below the ~ 30 mJy flux density limits of both the PMN and Greenbank radio surveys. This means that the true distribution of radio-excess objects is more densely populated at low radio excesses close to the radio/FIR correlation than is indicated by Fig. 2(a).

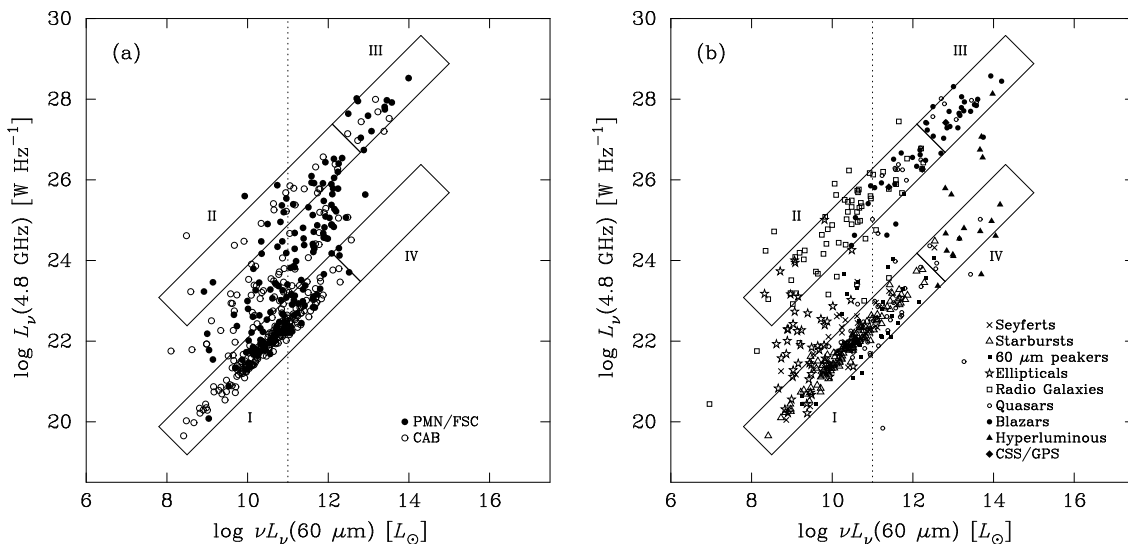


Fig. 2.— (a) Radio/FIR luminosity diagram for the PMN/FSC sample (*solid symbols*) and the CAB sample (*open symbols*). The vertical dotted line at $\nu L_\nu(60 \mu\text{m}) = 10^{11} L_\odot$ separates the low and high FIR luminosity samples. The four rectangular regions are discussed in the text. (b) Radio/FIR luminosity diagram for the starburst and active galaxy samples listed in Table 2.

The comparison objects shown in Fig. 1(b) are replotted in the radio/FIR luminosity diagram in Fig. 2(b). We identify four regions in Fig. 2(b) based on the locations of these objects; i) the sequence of radio-quiet objects on the radio/FIR correlation, ii) the apparent sequence of 3C radio galaxies and radio-loud quasars, iii) an extension of the radio-loud sequence to $\nu L_\nu(60 \mu\text{m}) \gtrsim 10^{12} L_\odot$ that is occupied predominantly by blazars, and iv) hyperluminous *IRAS* galaxies forming an extension of the radio-quiet sequence to $\nu L_\nu(60 \mu\text{m}) \gtrsim 10^{12} L_\odot$. The dominant source of both the radio and FIR luminosity from starburst objects in region i) is believed to be related to star formation. This group also includes radio-quiet quasi-stellar objects (QSO) for which there is less consensus on the origin of the radio and FIR luminosity. As mentioned above, the apparent correlation of objects in region ii) parallel to the radio-quiet correlation is likely to be due to the high flux density limit of the 3C catalog, rather than to a real correlation between the radio and FIR luminosities. AGN dominate the radio luminosity from these objects. The radio emission from the blazars in region iii) is believed to be relativistically beamed towards Earth, so isotropic luminosities over-estimate the true luminosity. The FIR emission from these objects may also be non-thermal and possibly beamed. The hyperluminous galaxies in region iv) include *IRAS* F10214+4724 and the Cloverleaf quasar, both of which are gravitationally lensed (Broadhurst & Lehar 1995; Magain et al. 1988). These objects are rare, either because of their extreme intrinsic luminosities or because gravitational lensing of the required magnification is rare. Indeed, no objects are present in this region of Fig. 2(a). Radio-intermediate objects are represented in Fig. 2(b), but only in significant numbers at luminosities below $\nu L_\nu(60 \mu\text{m}) \sim 10^{11.5} L_\odot$. Again, it is clear that only the Sadler (1984) nearby elliptical galaxies significantly populate the radio-intermediate region, with a few radio galaxies and Seyfert galaxies also extending into this region. The nearby elliptical galaxies are generally low luminosity objects with $\nu L_\nu(60 \mu\text{m}) < 10^{10.5} L_\odot$. There are few radio-intermediate objects in the comparison samples with $\nu L_\nu(60 \mu\text{m}) \gtrsim 10^{11.5} L_\odot$. This reinforces the suggestion that the high FIR luminosity radio-intermediate objects in Fig. 2(a) are a previously unrecognized population. Since most of the radio-excess objects have similar $60 \mu\text{m}$ flux densities slightly above the FSC limit, the high luminosity examples must all be at significant distances; an object with $S_\nu(60 \mu\text{m}) < 1 \text{ Jy}$ and $\nu L_\nu(60 \mu\text{m}) > 10^{11.5} L_\odot$ must be at redshift $z > 0.075$ in the adopted cosmology. These moderate redshift objects appear not to have been detected in previous surveys.

3.2. Radio-Excess Objects

We select a subsample of the radio-excess objects from the PMN/FSC sample based on the ratio of their FIR and radio fluxes, $u = \log [S_\nu(60 \mu\text{m})/S_\nu(4.8 \text{ GHz})]$ (CAB). Objects on the radio-quiet radio/FIR correlation have $u = 2.5 \pm 0.7$. Radio-excess objects were defined by Yun et al. (2001) to have radio emission more than five times larger than the radio/FIR correlation (i.e., star formation contributes $< 20\%$ of the radio emission from these objects). We adopt this criterion, which corresponds to values of $u < 1.8$. Objects that are traditionally classed as radio-loud have $u \leq 0.0$. We refer to objects with $0.0 < u < 1.8$ as radio-intermediate objects. These objects lie between the radio-quiet and radio-loud regions marked in Fig. 2. We focus on the nature of the radio-excess objects in the remainder of the paper.

The radio-excess sample contains 98 PMN/FSC objects and 109 CAB objects with $u < 1.8$. These are listed in Table 3. Column 1 gives the FSC name. Column 2 indicates the sample from which the object was selected. Column 3 lists the radio excess parameter, u . Columns 4 and 5 list the object luminosities at $60 \mu\text{m}$ and 4.8 GHz . Columns 6, 7 and 8 list the radio spectral indices between 3 cm and 6 cm , between 6 cm and 20 cm , and between 6 cm and 36 cm , respectively. We use our 3 cm and 6 cm flux densities obtained with the *ATCA*. The 20 cm flux densities are from the NVSS. The 36 cm flux densities are from the 843 MHz Sydney University Molongolo Sky Survey (Mauch et al. 2003, SUMSS). In all cases, the spectral index is defined as $S_\nu \propto \nu^\alpha$. Column 9 lists the projected linear size of the

radio source measured from our *ATCA* maps or taken from the literature. Column 10 lists the reference from which this value has been derived. Column 11 describes the object type. Column 12 lists the object identifications as given in Column 13 of Table 1.

Identification charts for the PMN/FSC radio-excess objects are presented in Fig. 3 where we indicate the radio position, *IRAS* 1σ and 3σ error ellipses, and our optical identification. Identification charts for some CAB objects were given in that paper.

Table 3. Radio-Excess Objects

FSC Name	Origin	u	$\log \nu L_\nu (60 \mu\text{m})$ (L_\odot)	$\log L_\nu (4.85 \text{ GHz})$ (W Hz^{-1})	$\alpha_{3-6\text{cm}}$	$\alpha_{6-20\text{cm}}$	$\alpha_{6-36\text{cm}}$	Radio Size (kpc)	Ref	Object Type	Identification
(1)	(2)	(3)	(4)	(5)	(6)	(7)	(8)	(9)	(10)	(11)	(12)
F00022+1231	CAB	-0.181	11.770	25.773	...	1.53	...	921.0	8	...	PKS 0002+12
F00123-2356	PMN	0.621	10.960	24.185	-1.68	-0.42	...	72.9	1	...	Abell 14
F00129+1422	CAB	0.499	-0.62	E	...
F00183-7111	PMN	1.042	12.918	25.635	-1.25	...	-0.78	<5.8	1	ULIRG	IRAS 00182-7112
F00349+0916	CAB	1.046	-0.82	UGC 00373
F00460+3141	CAB	0.721	10.219	23.372	...	-0.14	...	<1.3	9	S0	NGC 262
F00550+3004	CAB	-0.829	9.674	24.376	...	0.69	...	1749.6	12	E, FR I	NGC 315
F00567+2647	CAB	0.969	10.906	23.799	...	-0.37	...	40.0	12	...	IC 64
F01009-3241 ^a	PMN	0.485	12.081	25.378	-1.61	-1.46	-1.45	<5.0	1	...	PKS 0100-326
F01044-4050	PMN	-0.921	12.987	27.590	0.45	4.5	29	QSO	Q0104-408
F01046+3208	CAB	-0.691	9.913	24.477	...	0.54	...	172.0	12	S0	NGC 383
F01264-5705	PMN	0.254	10.742	24.342	0.85	...	0.22	<1.7	1	variable	...
F01317-3644	CAB	-0.394	10.959	25.221	...	1.08	...	7.2	1	S0-a	NGC 612
F01348+3254	CAB	-0.879	12.817	27.441	...	-0.85	...	<4.2	24	CSS QSO	3C 48
F01475-0740	PMN	0.709	10.287	23.452	...	-0.35	...	<7.6	8	E-S0	IRAS 01475-0740
F01477-1655	PMN	0.744	11.641	24.713	-0.43	-0.68	...	<6.9	1	...	PKS B0147-169
F02358+1623	CAB	-0.869	13.231	27.687	...	-0.09	...	<0.008	17	BL Lac	PKS 0235+164
F02367+0052	PMN	0.693	9.000	22.184	...	0.55	...	<3.9	8	Sa	NGC 1032
F02386-0828	PMN	-0.439	9.142	23.459	...	0.80	...	<2.2	8	E	NGC 1052
F02419-5625	PMN	0.241	10.861	24.475	-0.47	...	-0.01	<1.6	1
F02470-3130	PMN	0.881	9.662	22.654	-0.12	-0.18	-0.81	<0.3	1	...	IC 1858
F02474+4127	CAB	1.409	10.175	22.641	...	-0.82	...	<1.3	9	S0	NGC 1106
F02483+4302	CAB	0.454	11.790	25.195	...	0.12	...	<5.5	13	(Q+2G)	GC 0248+430
F02483-5456	PMN	0.199	12.243	25.781	-0.96	...	-0.82	<1.3	1
F03079-3031	PMN	-0.288	10.816	24.957	...	-0.66	...	1250.7	8	E	PKS B0307-305
F03088-0906	PMN	1.725	10.567	22.718	...	-0.73	...	<0.04	31	...	Arp 304
F03164+4119	CAB	-0.773	11.145	25.791	...	0.50	...	>15.9	27	Pec.	NGC 1275
F03169+1850	CAB	-0.447	12.172	26.387	-0.28	0.50	...	<1.3	6	...	OE +129
F03265-2852	PMN	0.025	11.509	25.320	-0.92	-0.97	...	44.6	1	...	PKS B0326-288
F03384-2129	PMN	-0.547	10.496	24.905	-0.03	-0.21	...	<1.3	1	BL Lac	PKS B0338-214
F04023-1638	PMN	1.753	10.098	22.215	-3.43	-1.37	...	<0.7	1
F04137-1144	PMN	0.864	11.403	24.383	-1.01	-0.27	...	<3.6	1	...	IRAS 04136-1144
F04207-0127	PMN	-0.919	13.455	27.972	...	0.25	...	0.01	35	Blazar	PKS 0420-014
F04305+0514	PMN	-0.434	10.897	25.198	...	0.01	...	>761.2	34	S0, Sy 1	3C 120
F04367-2726	PMN	1.114	11.633	24.354	-0.86	-0.87	...	9.1	1	...	IRAS 04367-2726
F04500-0311	PMN	0.877	9.998	22.996	...	0.00	...	>6.4	8	E	NGC 1684
F05212-3630	PMN	-1.272	10.737	25.866	-0.68	-0.81	...	12.9	1	N	Q0521-365
F05246+0103 ^b	PMN	1.145	12.139	24.834	...	1.92	...	<1.2	13	GPS	IRAS 05246+0103
F05265-4720	PMN	1.274	11.989	24.542	1.83	<3.1	1	...	IRAS 05265-4720
F05373-4406	PMN	-0.738	13.404	27.746	0.07	92.0	7	BL Lac	PKS 0537-441
F05497-0728	PMN	1.404	10.132	22.606	...	-0.49	...	0.9	33	S0, Sy 2	NGC 2110

Table 3—Continued

FSC Name	Origin	u	$\log \nu L_\nu(60 \mu\text{m})$ (L_\odot)	$\log L_\nu(4.85 \text{ GHz})$ (W Hz^{-1})	$\alpha_{3-6\text{cm}}$	$\alpha_{6-20\text{cm}}$	$\alpha_{6-36\text{cm}}$	Radio Size (kpc)	Ref	Object Type	Identification
(1)	(2)	(3)	(4)	(5)	(6)	(7)	(8)	(9)	(10)	(11)	(12)
F05511+4625	CAB	1.543	10.892	23.220	...	-0.84	...	2.2	28	SB...	UGC 03374
F05576+6522	CAB	1.280	10.119	22.713	...	-0.22	...	<2.2	12	Sa:	UGC 03386
F05585-5026	PMN	0.392	11.376	24.809	-0.25	<1.6	1	QSO	Q0558-504
F06065-7934	PMN	-0.189	12.239	26.199	-1.09	...	-0.85	<5.4	1	...	PKS 0606-796
F06090-1922	PMN	1.160	11.167	23.833	-0.52	-2.04	...	25.0	1	QSO	...
F06098+7103	CAB	1.029	10.649	23.495	...	-0.92	...	<1.2	9	S0:	UGC 03426
F06195-4503	PMN	-0.245	11.869	25.914	-0.43	<3.1	1	...	PKS B0619-450
F06343-2032	CAB	-0.877	10.946	25.681	...	0.61	...	1266.5	8	E, FR II	PKS 0634-20
F06374-7513	PMN	-1.553	12.737	27.953	-0.26	...	0.11	<7.8	1	QSO	Q0637-752
F06457+7429	CAB	1.012	10.392	23.252	...	-0.68	...	<2.7	9	S0-a	IC 450
F07144+4410	CAB	0.926	10.787	23.717	...	-0.34	...	<25.6	8
F07157+4039	CAB	1.309	0.35
F07162+7126	CAB	-0.522	0.07	BL Lac	S5 0716+71
F07224+3003	CAB	1.666	10.793	23.000	...	-0.65	...	15.8	14	...	A0722+30
F07325+2517	CAB	0.567	-0.71	E	...
F07352+1749	CAB	-0.934	12.482	27.144	...	-0.03	...	18.8	25	BL Lac	PKS 0735+17
F07543+1004	PMN	-0.573	12.809	27.043	...	-0.17	...	14.1	18	BL Lac	PKS 0754+100
F07552+1449	CAB	1.165	10.713	23.408	...	-0.81	...	120.0	8
F08014+0515	PMN	1.529	10.293	22.640	...	-0.57	...	<1.1	12	Sy 2	UGC 04203
F08064-1018	PMN	-0.511	11.585	25.932	-0.82	-0.73	...	345.0	1	N, FR II	3C 195
F08079+2822	CAB	0.781	-1.49	Empty field	...
F08147+3137	CAB	1.208	11.774	24.396	...	-0.48	...	44.0	8
F08291+0439	PMN	-0.698	11.930	26.437	...	0.44	...	114.7	3	BL Lac	Q0829+046
F08352+2504	CAB	1.126	10.312	23.055	...	-0.57	...	0.5	32	...	NGC 2622
F08369+2959	CAB	0.226	11.044	24.672	...	-0.68	...	619.4	15	...	Zw 0837+30
F08400+5023	CAB	1.675	10.136	22.337	...	-0.81	...	<1.3	12	Sa?	NGC 2639
F08519+2017	CAB	-0.480	12.731	26.976	...	0.46	...	0.6	2	BL Lac	OJ 287
F08544+2100	CAB	1.435	10.665	23.098	...	-0.92	...	<13.8	8
F08563+6058	CAB	1.062	-0.81
F09067+1940	CAB	0.364	10.026	23.531	...	0.37	...	<11.6	8	...	Mrk 1226
F09136+0043	CAB	0.724	-1.05	Empty field	...
F09165-0726	PMN	0.233	12.102	25.645	...	-0.27	...	<78.6	8
F09173+7203	CAB	1.256	9.645	22.265	...	0.05	...	<1.3	12	E	NGC 2810
F09253-3412	PMN	1.012	11.877	24.675	-1.23	-0.68	...	<3.1	1	QSO	...
F09288+7229	CAB	1.385	-0.99
F09311+1022	CAB	0.477	9.104	22.504	...	0.21	...	<0.9	12	...	NGC 2911
F09323+0732	PMN	-0.133	12.146	26.049	...	-0.18	...	<80.8	8	...	OK+052
F09359+3554	CAB	0.794	9.671	22.750	...	-0.92	...	34.0	8
F09416-0137	PMN	1.224	11.943	24.554	...	-0.19	IRAS 09415-0137
F09446+1359	CAB	1.237	11.174	23.787	...	-0.41	...	<28.0	8	Sy 1.9	...
F09589+2901	CAB	-0.826	11.687	26.320	...	-1.04	...	506.5	10	N, FR II	3C 234

Table 3—Continued

FSC Name	Origin	u	$\log \nu L_\nu(60 \mu\text{m})$ (L_\odot)	$\log L_\nu(4.85 \text{ GHz})$ (W Hz^{-1})	$\alpha_{3-6\text{cm}}$	$\alpha_{6-20\text{cm}}$	$\alpha_{6-36\text{cm}}$	Radio Size (kpc)	Ref	Object Type	Identification
(1)	(2)	(3)	(4)	(5)	(6)	(7)	(8)	(9)	(10)	(11)	(12)
F10170+6451	CAB	1.021	12.087	24.886	...	-1.01	...	<52.0	8
F10227-8251	PMN	1.067	11.203	23.982	-1.26	...	-0.63	32.1	1	...	IRAS 10227-8251
F10418+1153	CAB	0.438	11.940	25.293	...	-0.55	...	102.0	10
F10560-0219	PMN	1.453	10.988	23.401	...	-1.20	IRAS 10560-0219
F11085+2858	CAB	1.777	11.287	23.379	...	0.86	...	44.5	12	Dbl Sys	NGC 3561
F11220+3902	CAB	1.593	9.690	21.975	...	-0.67	...	<3.0	12	E-S0	NGC 3665
F11243-2244	PMN	0.668	11.728	24.872	-1.02	-0.93	...	<3.8	1
F11270+0031	CAB	-0.177	11.796	25.771	...	-0.85	...	87.7	36	...	4C +00.40
F11412+2014	CAB	1.752	10.630	22.749	...	-0.56	...	18.0	12	Irr	UGC 06697
F11445-3755	PMN	-0.840	13.399	27.809	0.38	0.09	...	<3.4	1	BL Lac	PKS 1144-379
F11494+7053	CAB	0.953	-0.47
F11553+5543	CAB	0.713	8.622	21.788	...	-0.12	...	<0.5	12	S0	NGC 3998
F12173-3541	PMN	1.276	11.631	24.212	-1.02	-0.70	...	<0.8	1	...	ESO 380-IG015
F12176+2933	CAB	0.227	8.101	21.754	...	-0.12	...	<1.0	12	E	NGC 4278
F12183-1015	PMN	0.644	12.153	25.276	-0.34	-0.23	...	<5.5	1
F12206+5843	CAB	0.523	9.591	22.942	...	-0.34	...	13.8	9	E	NGC 4335
F12225+1309	CAB	-0.756	8.591	23.226	...	-0.60	...	<2.0	12	S0	NGC 4374
F12252+1317	CAB	1.768	9.521	21.633	...	0.11	...	1.2	9	...	NGC 4438
F12265+0219	PMN	-1.326	12.497	27.640	...	-0.19	QSO	3C 273
F12282+1240	CAB	-2.250	8.485	24.614	...	-0.55	...	89.0	26	...	M87
F12287+6605	CAB	0.647	-0.66
F12373+2229	CAB	0.309	-1.07	E	PKS 1237+22
F12374-1120	PMN	1.477	9.141	21.544	0.05	0.09	...	<0.06	11	Sa	M104, NGC 4594
F12440-2531	PMN	-0.467	13.074	27.207	0.20	0.02	...	<1.6	1	QSO	Q1244-255
F12535-0530	PMN	-1.618	12.706	28.018	...	0.06	Blazar	3C 279
F12597+1643	CAB	1.165	12.484	25.072	...	-0.63	...	<89.0	10
F13059-2406	PMN	0.812	10.200	23.263	-0.91	-0.62	...	<0.4	1	Sy 2	IRAS 13059-2407
F13080+3237	CAB	-0.430	13.511	27.522	...	-0.32	...	321.3	3	Blazar	Q1308+326
F13174-1651 ^c	PMN	1.083	10.012	22.801	-0.41	-1.20	...	5.5	1	Dbl Sys	VV 802
F13184+0914	CAB	1.595	11.102	23.375	...	-0.50	...	<3.6	12	Dbl sys	NGC 5100
F13197-1627	PMN	1.755	10.962	23.081	-1.08	-0.79	...	<0.5	1	...	MCG-03-34-063
F13334-0814	PMN	0.052	10.349	24.169	...	0.80	S0-a	NGC 5232
F13384+4503	CAB	0.517	0.18
F13443+1439	CAB	1.619	10.973	23.225	...	-0.67	...	41.8	10	...	Zw 102.056
F13451+1232	CAB	-0.208	12.232	26.271	...	-0.45	...	0.3	24	GPS	PKS 1345+12
F13468+4013	CAB	0.946	9.333	22.265	...	-0.36	...	<0.8	12	S0-a	NGC 5311
F13475+6026	CAB	0.935	8.987	21.930	...	-0.41	...	3.4	12	E	NGC 5322
F13500+3141	CAB	-0.739	10.655	25.255	...	-0.60	...	282.0	5	FR II	3C 293
F13513+4031	CAB	0.932	8.980	21.926	...	-0.12	...	15.3	12	S0+S0	NGC 5353/4
F13514+6556	CAB	0.626	-0.52
F13536+1836	CAB	1.298	11.507	24.069	...	-1.00	...	27.0	21	...	Mrk 463

Table 3—Continued

FSC Name	Origin	u	$\log \nu L_\nu(60 \mu\text{m})$ (L_\odot)	$\log L_\nu(4.85 \text{ GHz})$ (W Hz^{-1})	$\alpha_{3-6\text{cm}}$	$\alpha_{6-20\text{cm}}$	$\alpha_{6-36\text{cm}}$	Radio Size (kpc)	Ref	Object Type	Identification
(1)	(2)	(3)	(4)	(5)	(6)	(7)	(8)	(9)	(10)	(11)	(12)
F13536+0529	PMN	1.146	9.045	21.779	...	-0.23	...	<0.5	9	...	NGC 5363
F14003+2846	CAB	1.030	0.26
F14047+2841	CAB	-0.521	11.406	25.776	...	0.87	...	<31.8	10	BL Lac	OQ 208
F14106-0258	CAB	1.682	10.235	22.432	...	-0.53	...	0.6	31	Sa pec, Sy	NGC 5506
F14111+0753	PMN	1.426	10.616	23.061	...	-0.88	...	10.9	8	Dbl Sys	NGC 5514
F14165+0642	PMN	-0.846	13.577	27.918	...	-1.11	...	12.8	24	CSS QSO	3C 298
F14180+5437	CAB	-0.906	11.874	26.569	...	0.62	...	205.4	10	BL Lac	OQ 530
F14263+2737	CAB	0.280	9.579	23.173	...	0.77	...	<1.3	12	...	NGC 5635
F14271+1048	CAB	1.011	10.352	23.206	...	0.79	...	<5.0	12	Sb-c	UGC 09309
F14306+3631	CAB	0.465	9.735	23.145	...	0.25	...	<7.4	9	...	NGC 5675
F14354+3024	CAB	0.854	-0.59
F14381-3901	PMN	0.315	11.616	25.127	-0.49	1.28	...	<3.2	1
F14390+5343	CAB	1.687	11.034	23.212	...	-0.65	...	<15.0	8	...	Mrk 477
F14474+4233	CAB	0.524	11.897	25.183	...	-0.20	...	<68.7	10
F14483+6328	CAB	-0.718	10.338	24.919	...	-0.84	...	4.8	12	SB0	IC 1065
F14501+0639	PMN	0.115	12.121	25.784	...	-0.23	...	<77.0	10
F14565-1629	PMN	1.131	10.688	23.433	-1.11	-0.76	...	<0.3	1	Sb	NGC 5793
F14592+1336	CAB	0.794	-1.56	Empty field	...
F15067+0913	CAB	1.293	10.893	23.462	...	-0.27	...	<19.0	10	...	Zw 077.021
F15129+0432	PMN	1.050	11.618	24.409	...	-0.55	...	<35.0	8	...	IRAS 15129+0432
F15151+3404	CAB	0.394	-0.55
F15284+3808	CAB	-0.026	0.33
F15295+2414	CAB	-0.102	11.732	25.676	...	1.46	...	740.9	10	Pec	3C 321.0
F15306-0832	PMN	1.276	10.770	23.365	...	-0.58	Sy 2	MCG-01-40-001
F15366+1711	CAB	0.058	10.097	23.907	...	1.95	...	19.7	9	S0-a	NGC 5972
F15366+0544	PMN	0.220	10.145	23.795	...	0.31	E	MCG+01-40-010
F15471+2158	CAB	0.640	10.164	23.389	...	-0.96	...	<4.1	12	Chain	UGC 10049
F15494-7905	PMN	-0.559	12.141	26.521	-0.72	...	-0.29	0.5	30	NLRG	PKS 1549-79
F15599+0206	PMN	-0.670	11.585	26.093	...	-0.64	...	761.4	20	FR II NLRG	3C 327
F16022+1753	CAB	0.665	10.865	24.063	...	0.32	...	35.8	12	Dbl Sys	NGC 6040
F16159-0402	PMN	1.171	12.439	25.066	...	-0.93	IRAS 16159-0402
F16254-6735	PMN	1.471	10.868	23.261	-0.75	...	-0.67	<0.4	1	...	IRAS 16254-6735
F16268+5152	CAB	0.975	10.772	23.654	...	-0.09	...	<22.9	8	...	Mrk 1498
F16314+3526	CAB	0.818	10.091	23.139	...	-0.69	...	<4.0	12	...	NGC 6185
F16319+4725	CAB	1.102	11.683	24.414	...	-0.31	...	<46.7	8
F16328+2055	CAB	1.256	0.42
F16413+3954	CAB	-1.144	13.173	27.996	...	0.13	...	33.8	3	QSO	3C 345
F16431+0217	PMN	-0.421	11.131	25.394	...	-0.89	...	<35.6	8	E	4C +02.42
F17179+5444	CAB	1.024	12.254	25.052	...	-0.76	...	<58.0	8
F17326+3859	CAB	-0.233	13.384	27.202	...	-0.28	BL Lac QSO	B2 1732+389
F17345+1124	CAB	1.141	11.905	24.579	...	-1.00	...	<55.0	8

Table 3—Continued

FSC Name	Origin	u	$\log \nu L_\nu(60 \mu\text{m})$ (L_\odot)	$\log L_\nu(4.85 \text{ GHz})$ (W Hz^{-1})	$\alpha_{3-6\text{cm}}$	$\alpha_{6-20\text{cm}}$	$\alpha_{6-36\text{cm}}$	Radio Size (kpc)	Ref	Object Type	Identification
(1)	(2)	(3)	(4)	(5)	(6)	(7)	(8)	(9)	(10)	(11)	(12)
F17406+1613	CAB	0.212	10.199	23.858	...	-0.55	...	<1.3	9	Dbl Sys	UGC 10950
F17473+4401	CAB	0.476	-0.94
F17490+2659	CAB	0.905	11.775	24.692	...	-0.72	...	<57.2	8
F17537+1820	CAB	0.562	9.621	22.936	...	-0.03	...	<5.6	9	...	NGC 6500
F18072+6948	CAB	-0.909	10.642	25.410	...	0.12	...	233.0	9	BL Lac	UGC 11130
F18146+4238	CAB	1.297	-0.93	Dbl Sys	UGC 11185
F18325-5926	PMN	1.689	10.832	23.016	-1.02	...	-0.80	<0.3	1	Sy 2	Fairall 90
F19254-7245	PMN	1.764	12.085	24.176	-0.86	...	-0.61	<0.5	1	Dbl Sys	Superantennae
F19497+0222	PMN	-0.720	10.962	25.538	...	-0.12	...	170.6	4	FR II	3C 403
F20057-4858	PMN	-0.666	10.850	25.367	-0.13	<1.8	1	BL Lac QSO	Q2005-489
F20203-5733	PMN	-0.445	12.345	26.540	-1.14	...	-1.08	328.3	1	...	PKS 2020-57
F20482-5715	PMN	1.161	10.565	23.280	-1.05	...	-0.98	1.3	23	...	IC 5063
F20517-5809	PMN	0.890	11.907	24.821	-0.68	...	0.06	<4.1	1
F21139-6613	PMN	1.180	11.655	24.294	-1.22	...	-0.88	<3.5	1
F21309-0726	PMN	0.723	11.168	24.290	-0.99	-0.90	...	<2.2	99
F21356-1015	PMN	0.995	12.083	24.887	-0.92	-0.86	...	<9.1	99	...	IRAS 21356-1015
F21497-0824	PMN	1.682	11.330	23.515	...	-0.81	IRAS 21497-0824
F21511-4606	PMN	0.665	11.389	24.546	-0.28	<1.4	1
F21527-2856	PMN	0.202	11.890	25.478	-0.79	-0.67	...	<2.3	1
F21529-6955	PMN	-1.799	9.930	25.598	-0.73	58.2	16	FR II	PKS 2153-69
F21583-3800	PMN	-0.266	10.340	24.473	...	-0.73	FR II	PKS 2158-380
F22006+4202	CAB	-0.950	11.050	25.852	...	-0.42	...	28.6	3	BL Lac	BL Lac
F22045+0959	CAB	1.797	11.085	23.157	...	-0.73	...	<11.6	8	...	NGC 7212
F22061-4724	PMN	1.241	9.736	22.373	-0.15	<0.2	9	...	NGC 7213
F22073-4044	PMN	0.054	-0.90	1	...	PKS B2207-407
F22175+2558	CAB	-0.352	11.179	25.377	...	1.08	...	443.0	8
F22231-0512	PMN	-1.029	13.993	28.522	...	-0.12	Blazar	3C 446
F22521-3929	PMN	-0.032	12.079	25.892	-0.94	-1.11	...	68.3	1	...	PKS 2252-394
F22537-6512	PMN	0.807	12.031	25.056	-0.92	...	-0.82	9.0	1	...	PKS 2253-652
F22544-3643	PMN	-0.432	8.920	23.230	-0.36	-0.01	0.03	<0.02	1	...	IC 1459
F22559+0733	CAB	1.336	-0.16
F23002-5828	PMN	1.116	11.888	24.570	-0.86	...	-0.66	<3.9	1
F23075-5957	PMN	0.665	11.932	25.091	0.23	...	0.42	<6.5	1	...	IRAS 23075-5957
F23135-4745	PMN	-0.200	12.883	26.739	-0.90	47.4	1	QSO	PKS 2313-477
F23140+0348	PMN	-0.350	12.259	26.404	...	-1.00	...	40.6	22	N, CSS gal.	3C 459
F23389+0300	PMN	0.799	12.195	25.219	...	-1.19	...	<49.9	8	...	PKS 2338+03
F23400-8705	PMN	0.324	11.169	24.682	-1.12	...	-0.78	<2.6	1	...	PKS 2340-870
F23439+4007	CAB	0.791	0.38
F23475-7407	PMN	1.084	11.064	23.819	-0.25	...	-1.17	6.4	1
F23493-0126	PMN	-0.456	11.650	25.918	...	-0.68	N, FR II	Q2349-014
F23532+2956	CAB	0.902	10.583	23.548	...	-0.89	...	<13.6	8	...	Zw 2353+29

Table 3—Continued

FSC Name	Origin	u	$\log \nu L_\nu(60 \mu\text{m})$ (L_\odot)	$\log L_\nu(4.85 \text{ GHz})$ (W Hz^{-1})	$\alpha_{3-6\text{cm}}$	$\alpha_{6-20\text{cm}}$	$\alpha_{6-36\text{cm}}$	Radio Size (kpc)	Ref	Object Type	Identification
(1)	(2)	(3)	(4)	(5)	(6)	(7)	(8)	(9)	(10)	(11)	(12)
F23557+1654	CAB	1.254	-0.64
F23565-7631	PMN	1.133	11.145	23.859	-0.51	...	-0.34	<0.6	1

^aCAB position is correct, but identification chart is incorrect.

^bGPS source discussed by Crawford et al. (1996).

^cGalaxy pair, both radio sources. Tabulated radio fluxes and optical position are for eastern galaxy. $S_\nu(4.8 \text{ GHz}) = 17.4 \text{ mJy}$ and $S_\nu(8.6 \text{ GHz}) = 13.6 \text{ mJy}$ and $13^h 20^m 04^s .7 -17^\circ 07' 17''$ for western galaxy.

References. — (1) Our ATCA data; (2) Altschuler et al. 1995; (3) Antonucci & Ulvestad 1985; (4) Black et al. 1992; (5) Bridle, Fomalont, & Cornwell 1981; (6) Browne et al. 1998; (7) Cassaro et al. 1999; (8) Condon et al. 1995; (9) Condon & Broderick 1988; (10) Condon & Broderick 1991; (11) Condon et al. 1982; (12) Condon et al. 1991b; (13) Crawford et al. 1996; (14) Fanti et al. 1986; (15) Fanti et al. 1987; (16) Fosbury et al. 1998; (17) Gabuzda & Cawthorne 2000; (18) Ghosh & Soundararajaperumal 1995; (19) Hutchings et al. 1994; (20) Leahy et al. 1997; (21) Mazzarella et al. 1991; (22) Morganti et al. 1999a; (23) Morganti et al. 1999b; (24) O’Dea 1998; (25) O’Dea, Barvainis, & Challis 1988; (26) Owen, Eilek, & Kassim 2000; (27) Pedlar et al. 1990; (28) Schmitt et al. 2001; (29) Shen et al. 1997; (30) Tadhunter et al. 2001; (31) Thean et al. 2000; (32) Ulvestad 1986; (33) Ulvestad & Wilson 1983; (34) Walker, Benson, & Unwin 1987; (35) Wehrle et al. 1992; (36) FIRST image via NED. Published angular sizes were converted to linear sizes using $H_0 = 50 \text{ km s}^{-1} \text{ Mpc}^{-1}$ and $q_0 = 0.5$.

Fig. 3.— **Please note: Figures 3a – d are provided separately in GIF format.** Identification charts for the radio-excess PMN/FSC objects taken from DSS red images. Crosses mark radio sources (PMN, *ATCA* or NVSS). Solid and dashed ellipses indicate the *IRAS* 1σ and 3σ positional uncertainties, respectively. Circles mark the positions of the optical identifications. Each chart is 3 arcmin on a side with North up and East to the left. The linear scale at the object corresponding to an angle of 1 arcmin is shown at lower right. The object redshift is listed at lower left.

4. Well-Studied Objects in the Radio-Excess Sample

Several well-studied objects are present in the radio-excess sample. While it is not possible to generalize about the nature of all radio-excess objects from the properties of a few, their presence does provide some insight into the types of objects that constitute the radio-excess population. The well-studied radio-excess objects are all AGN of various types including interacting Seyfert galaxies, CSS/GPS and double-lobed radio galaxies, radio-loud quasars, and blazars. Their radio powers range over more than 6 orders of magnitude, and their radio sizes span the range from kpc-scale objects smaller than the host galaxy to Mpc-scale extended radio galaxies. Compact radio sources occur in both Seyfert galaxies, where the radio source has low power and small radio excess, and in CSS and GPS sources that have high radio powers and large radio excesses. The well-studied objects with extended radio structure all have large radio-excesses and high radio powers. The FIR luminosities of the well-studied radio-excess objects range over at least 4 orders of magnitude. AGN-dominated ultra-luminous infrared galaxies are present at high FIR luminosities. Most of these have large radio excesses. Only a few well-studied FIR-luminous objects have intermediate radio-excesses. At low FIR luminosities, elliptical galaxies with compact radio cores are common. Many of these have intermediate radio-excesses. We now consider each of these objects in detail.

4.1. Ultra-Luminous Infrared Galaxies

IRAS 00182-7112 (F00183-7111) is a high redshift ($z = 0.327$) ULIRG ($\nu L_\nu(60 \mu\text{m}) = 10^{12.8} L_\odot$). It is one of the few well-studied high FIR luminosity objects having an intermediate radio excess ($u = 1.04$). It is a powerful radio source ($L_\nu(4.8 \text{ GHz}) = 10^{25.6} \text{ W Hz}^{-1}$) that is unresolved in our $1''$ ATCA beam ($< 5.8 \text{ kpc}$) at 8.6 GHz. Norris et al. (1988) detected a compact radio core at 1.66 GHz using the Parkes-Tidbinbilla Interferometer. They measured a flux density of 250 mJy with fringe spacing $\sim 0.1''$, which corresponds to 578 pc. The flux density expected for the source at 1.66 GHz, derived from the observed ATCA flux density at 5 GHz and SUMSS flux density at 843 MHz, is 249 mJy. This strongly suggests that the radio source is compact, with total extent $< 578 \text{ pc}$. There is evidence for a weak or obscured AGN from the classification of the optical spectrum as a LINER (Armus, Heckman, & Miley 1989). Strong mid-infrared continuum and relatively weak polycyclic aromatic hydrocarbon ($7.7 \mu\text{m}$; PAH) emission indicate the presence of an obscured AGN (Tran et al. 2001).

4.2. Seyfert Galaxies

The Superantennae (F19254-7245) is an infrared luminous interacting pair of galaxies ($\nu L_\nu(60 \mu\text{m}) = 10^{12.05} L_\odot$). It has a small radio excess ($u = 1.76$) and moderate radio power ($L_\nu(4.8 \text{ GHz}) = 10^{24.2} \text{ W Hz}^{-1}$). The small radio excess is only just sufficient to distinguish it from radio-quiet objects. The two distinct nuclei have been classified as a Seyfert 2 (southern galaxy) and a starburst/LINER (northern galaxy) based on optical spectroscopy (Mirabel, Lutz, & Maza 1991). The Seyfert galaxy is the dominant radio source (ATCA data) and is likely to be the FIR source (Mirabel et al. 1991). The radio source is smaller than our ATCA beam at 8.6 GHz so must be $< 500 \text{ pc}$ in extent.

Mrk 463 (F13536+1836) contains two nuclei that are separated by $\sim 5.9 \text{ kpc}$ and embedded in a common envelope (Mazzarella & Boroson 1993). Both nuclei have Seyfert 2 optical spectra (Shuder & Osterbrock 1981) though the eastern nucleus, Mrk 463E, has a Seyfert 1 nucleus observed in polarized light (Veilleux, Sanders, & Kim 1997). Both nuclei are radio sources. Mrk 463E has a luminous steep-spectrum core and weak radio lobes with extent $\sim 27 \text{ kpc}$ (Mazzarella et al. 1991). Mazzarella et al. (1991) suggest Mrk 463E may be a transition object between the smaller, weaker radio sources seen in Seyfert

galaxies and extended powerful radio galaxies. At high resolution, the core is found to be a compact double with extent ~ 1.8 kpc (Thean et al. 2000). Mrk 463W has a weaker radio source with a flatter spectrum (Mazzarella et al. 1991). Overall, Mrk 463 appears in our sample as a moderately powerful radio source ($L_\nu(4.8 \text{ GHz}) = 10^{24.1} \text{ W Hz}^{-1}$) with high FIR luminosity ($\nu L_\nu(60 \text{ } \mu\text{m}) = 10^{11.5} L_\odot$) and an intermediate radio excess ($u = 1.30$).

NGC 7212 (F22045+0959) is a Seyfert 2 galaxy in an interacting triple (Wasilewski 1981). It has a small radio excess of $u = 1.80$ on the boundary with radio-quiet objects. The radio source is a compact double with a separation of ~ 520 pc (Falcke, Wilson, & Simpson 1998) and moderate radio power ($L_\nu(4.8 \text{ GHz}) = 10^{23.2} \text{ W Hz}^{-1}$). NGC 7212 is luminous in the FIR, having $\nu L_\nu(60 \text{ } \mu\text{m}) = 10^{11.1} L_\odot$.

NGC 2110 (F05497-0728) is a nearby X-ray luminous Seyfert 2 galaxy with an intermediate radio excess of $u = 1.40$. NGC 2110 has a small radio source with a low radio power of $L_\nu(4.8 \text{ GHz}) = 10^{22.7} \text{ W Hz}^{-1}$. The radio source consists of a compact flat-spectrum core and symmetric jets with a total extent of ~ 590 pc (Mundell et al. 2000). The optical host is an elliptical galaxy with an equatorial dust lane, which is indicative of a previous merger (Colbert, Mulchaey, & Zabludoff 2001), and a moderate FIR luminosity of $\nu L_\nu(60 \text{ } \mu\text{m}) = 10^{10.2} L_\odot$.

NGC 5506 (F14106-0258) is also a nearby X-ray luminous Seyfert 2 galaxy with a small radio excess of $u = 1.68$. The radio source has very low power ($L_\nu(4.8 \text{ GHz}) = 10^{22.4} \text{ W Hz}^{-1}$) and is small with an unresolved core and diffuse emission extending over ~ 500 pc (Thean et al. 2000). The host is an Sa galaxy with a moderate FIR luminosity of $\nu L_\nu(60 \text{ } \mu\text{m}) = 10^{10.2} L_\odot$.

IC 5063 (F20482-5715) has properties in common with both Seyfert galaxies and radio galaxies (Colina, Sparks, & Macchetto 1991). It is an X-ray bright Seyfert 2 galaxy, with intermediate radio excess ($u = 1.16$) and low radio power ($L_\nu(4.8 \text{ GHz}) = 10^{23.5} \text{ W Hz}^{-1}$). The radio emission arises from a compact double-lobed source 1.3 kpc in extent (Morganti et al. 1999b). The host galaxy is a nearby elliptical with dust lanes, so it has probably undergone a recent merger. The galaxy has a moderate FIR luminosity of $\nu L_\nu(60 \text{ } \mu\text{m}) = 10^{10.6} L_\odot$.

4.3. LINERs

M104 (F12374-1120, Sombrero Galaxy, NGC 4594) is a well-known edge-on disk galaxy with a large bulge. It has an intermediate radio excess of $u = 1.50$ and very low radio power of $L_\nu(4.8 \text{ GHz}) = 10^{21.9} \text{ W Hz}^{-1}$. It also has a low FIR luminosity of $\nu L_\nu(60 \text{ } \mu\text{m}) = 10^{9.4} L_\odot$. The optical emission-line spectrum is classified as a LINER and the optical continuum is dominated by an old stellar population (Kinney et al. 1993). Our *ATCA* observations show the GHz spectral slope to be slightly inverted. The radio source has a compact core less than 31 pc in extent (Thean et al. 2000), and extended radio emission that is weak relative to the central source and may be due to star formation or indirectly related to the AGN (Bajaja et al. 1988).

4.4. Ellipticals With Radio Cores

Several radio-excess galaxies belong to the sample of elliptical galaxies with radio cores studied by Slee et al. (1994) and mentioned in §3.1: NGC 612 (F01317-3644), NGC 1052 (F02386-0828), NGC 2110 (F05497-0728, discussed above), NGC 2911 (09311+1022), IC 5063 (F20482-5715, discussed above), NGC 7213 (F22061-4724), and IC 1459 (F22544-3643). The radio cores in elliptical galaxies were typically found by these authors to be extremely compact (unresolved on scales of a few parsecs) and to have a large range of radio powers ($L_\nu(4.8 \text{ GHz}) = 10^{21} - 10^{26} \text{ W Hz}^{-1}$). Their high-frequency spectral indices are

typically inverted or flat ($\langle \alpha \rangle \approx 0.3$, $S_\nu \propto \nu^\alpha$), due to absorption consistent with SSA or FFA. These objects have a range of radio power and radio excess, but low FIR luminosities ($\nu L_\nu(60 \mu\text{m}) < 10^{11} L_\odot$).

4.5. Radio Galaxies

3C 195 (F08064-1018, PKS 0806-10) is a high-power radio galaxy ($L_\nu(4.8 \text{ GHz}) = 10^{25.9} \text{ W Hz}^{-1}$) with a large radio excess ($u = -0.51$) that justifies its radio-loud classification. It has an FR II morphology (Fanaroff & Riley 1974) with a total extent of ~ 367 kpc (Morganti, Killeen, & Tadhunter 1993). The optical host is an asymmetric elliptical galaxy that appears to be interacting with a small less-luminous companion ~ 11 kpc (projected linear separation) from the nucleus. 3C 195 is a luminous FIR galaxy with $\nu L_\nu(60 \mu\text{m}) = 10^{11.5} L_\odot$.

3C 327 (F15599+0206, PKS 1559+02) is also a powerful FR II radio galaxy. It has $L_\nu(4.8 \text{ GHz}) = 10^{26.0} \text{ W Hz}^{-1}$ and a large radio excess of $u = -0.67$. The asymmetric radio lobes extend to ~ 768 kpc (Leahy et al. 1997). The optical host is a flattened elliptical with a Seyfert 2 nucleus. It is also a luminous FIR source with $\nu L_\nu(60 \mu\text{m}) = 10^{11.5} L_\odot$.

PKS 0634-20 (F06343-2032) is a radio galaxy with $L_\nu(4.8 \text{ GHz}) = 10^{25.7} \text{ W Hz}^{-1}$ and a very large radio excess ($u = -0.88$). It is an FR II with a total extent of nearly 1.3 Mpc (CAB). It has a strong high-ionization optical spectrum and an apparently normal elliptical host. The FIR luminosity is moderate with $\nu L_\nu(60 \mu\text{m}) = 10^{10.9} L_\odot$.

NGC 315 (F00550+3004) is a radio galaxy with a very large radio excess of $u = -0.83$, but with only moderate radio power ($L_\nu(4.8 \text{ GHz}) = 10^{24.4} \text{ W Hz}^{-1}$). It is a large FR I galaxy with a total extent of > 1.7 Mpc (Condon et al. 1991b). Evidence for superluminal motion has been detected in the radio source (Xu et al. 2000). The host is an elliptical galaxy with an equatorial dust disk and an unresolved optical nucleus (Capetti et al. 2000). It has a low FIR luminosity of $\nu L_\nu(60 \mu\text{m}) = 10^{9.7} L_\odot$.

3C 120 (F04305+0514) is a powerful radio galaxy ($L_\nu(4.8 \text{ GHz}) = 10^{25.4} \text{ W Hz}^{-1}$) with a large radio excess of $u = -0.43$. It has FR I morphology on large scales with a total extent of > 760 kpc (Walker et al. 1987). Superluminal motion has been detected in the small-scale radio structure and an optical and radio jet is observed on arcsecond scales. This object is highly variable at all wavelengths (radio – X-ray) and may be a blazar. The optical nucleus has a Seyfert 1 spectrum and the host galaxy may be disturbed. The FIR luminosity is moderate at $\nu L_\nu(60 \mu\text{m}) = 10^{10.9} L_\odot$.

NGC 1275 (F03164+4119, Perseus A) is the central cD galaxy in the Perseus cluster. It has a large radio excess ($u = -0.77$) and is luminous in both the radio and FIR with $L_\nu(4.8 \text{ GHz}) = 10^{25.8} \text{ W Hz}^{-1}$ and $\nu L_\nu(60 \mu\text{m}) = 10^{11.1} L_\odot$. The radio source has an asymmetric FR I morphology on kilo-parsec scales and complex morphology on smaller scales. It has a spiral companion at a separation of $\sim 3000 \text{ km s}^{-1}$ that may be infalling. The optical spectrum is classified as a Sy 1.5 but Véron (1978) has suggested the reclassification of this galaxy to a BL Lac due to its optical polarization and variability.

PKS 1549-79 (F15494-7905) is a powerful, compact, flat-spectrum radio source with $L_\nu(4.8 \text{ GHz}) = 10^{26.6} \text{ W Hz}^{-1}$ and a large radio excess of $u = -0.56$. It is a Narrow Line Radio Galaxy (NLRG) with a core-dominated core-jet morphology of total extent ~ 512 pc (Tadhunter et al. 2001). It is FIR luminous with $\nu L_\nu(60 \mu\text{m}) = 10^{12.08} L_\odot$. Tadhunter et al. (2001) argue that this is a young radio source that is intrinsically compact and embedded in a dense host galaxy interstellar medium, similar to CSS/GPS sources. They argue that the axis of radio emission is close to the line of sight, resulting in the observed flat radio spectrum, but that the quasar nucleus is highly obscured at optical wavelengths. The host galaxy is not well studied, but appears on Schmidt plates to be an elliptical with disturbed outer morphology (Jauncey et al. 1989).

M 87 (F12282+1240, NGC 4486, 3C 274) is a giant elliptical galaxy at the center of the Virgo cluster. It has the largest radio excess in the sample with $u = -2.25$. The radio source has moderate power with $L_\nu(4.8 \text{ GHz}) = 10^{24.6} \text{ W Hz}^{-1}$ and extended FR I morphology (Martel et al. 1999). The galaxy has a bright optical synchrotron jet and a LINER spectrum (Dopita et al. 1997). The FIR emission has low luminosity with $\nu L_\nu(60 \text{ } \mu\text{m}) = 10^{8.5} L_\odot$.

4.6. CSS/GPS Sources

PKS 1345+12 (F13451+1232, 4C 12.50) is a nearby radio-loud GPS galaxy with a radio excess of $u = -0.21$. The radio source is powerful ($L_\nu(4.8 \text{ GHz}) = 10^{26.3} \text{ W Hz}^{-1}$). The FIR emission is very luminous at $\nu L_\nu(60 \text{ } \mu\text{m}) = 10^{12.2} L_\odot$. The host galaxy is one of an interacting pair. The optical nuclei are separated by 4.3 kpc and are embedded in an asymmetric common envelope 43 kpc across (Heckman et al. 1986). The south-eastern elliptical galaxy was previously thought to be the radio source (Gilmore & Shaw 1986), but Hubble Space Telescope observations combined with high-resolution radio data have shown the radio emission to be associated with the north-western nucleus (Evans et al. 1999). This galaxy has a Seyfert 2 spectrum with a hidden broad-line region observed in the near-infrared (Veilleux et al. 1997). This object provides support for the scenario in which galaxy mergers produce high FIR luminosities and funnel gas to the nucleus to fuel an AGN (Sanders et al. 1988a). A high mass of molecular gas ($> 10^{10} M_\odot$) has been inferred from observations of H I absorption (Mirabel 1989) and CO emission (Evans et al. 1999). The CO emission is compact, suggesting the gas is concentrated around the nuclear region and provides fuel for the AGN (Evans et al. 1999). The continuum radio source is a two-sided jet with total extent $\sim 290 \text{ pc}$ (Lister et al. 2003). It is likely that the radio source is young, assuming that the jets are propagating at velocities similar to other compact symmetric objects (Lister et al. 2003). Evans et al. (1999, 2002) argue that the molecular gas is the source of fuel for the radio emission, as CO is only detected in the more radio-luminous nucleus in several interacting galaxy pairs. It is not clear, however, if the high molecular mass triggers or simply fuels the radio source. The detailed VLBI study of PKS 1345+12 by Lister et al. (2003) presents evidence that the radio jet is precessing, which suggests that the radio jet may have been triggered by the merger of two black holes, producing a spinning black hole.

3C 459 (F23140+0348) is a CSS galaxy with a large radio excess of $u = -0.35$. It is luminous at radio and FIR wavelengths with $L_\nu(4.8 \text{ GHz}) = 10^{26.4} \text{ W Hz}^{-1}$ and $\nu L_\nu(60 \text{ } \mu\text{m}) = 10^{12.2} L_\odot$. The radio source has a core and two lobes separated by 40 kpc. The host galaxy shows a post-starburst optical spectrum with blue continuum, young stellar absorption lines (Miller 1981), and nebular emission lines that Zheng et al. (1999) classified as a LINER. The host is an elliptical with disturbed morphology in the outer parts, possibly the remnant of multiple mergers (Zheng et al. 1999).

3C 48 (F01348+3254) is an extremely radio-loud ($u = -0.89$) CSS quasar. It is very luminous in both the radio and FIR with $L_\nu(4.8 \text{ GHz}) = 10^{27.4} \text{ W Hz}^{-1}$ and $\nu L_\nu(60 \text{ } \mu\text{m}) = 10^{12.7} L_\odot$. The radio source is small and consists of a flat-spectrum core and a bright steep-spectrum lobe (Wilkinson et al. 1991) with a total extent of $\sim 8 \text{ kpc}$ (Spencer et al. 1989). The host galaxy is overwhelmed at optical and near-infrared wavelengths by the quasar nucleus, but subtraction of the central source reveals disturbed outer isophotes indicative of a merger (Scoville et al. 2000; Stockton & Ridgway 1991). The optical spectrum is unusual for a quasar in that it shows strong Balmer absorption lines that indicate the presence of a dominant young stellar population (Boroson & Oke 1984).

3C 298 (F14165+0642) is also an extremely radio-loud ($u = -0.86$) CSS quasar. It is extremely luminous at radio and FIR wavelengths with $L_\nu(4.8 \text{ GHz}) = 10^{27.9} \text{ W Hz}^{-1}$ and $\nu L_\nu(60 \text{ } \mu\text{m}) = 10^{13.2} L_\odot$. The radio source has a compact triple morphology and the host galaxy may be disturbed.

4.7. Quasars

There are a number of known radio-loud quasars in the radio-excess sample: PKS 0104-408 (F01044-4050), Q0521-365 (F05212-3630), Q0558-504 (F05585-5026), Q0637-752 (F06374-7513), Q1244-255 (F12440-2531), 3C 345 (F16413+3954), PKS 2313-477 (F23135-4745), and Q2349-014 (F23493-0126). These objects all have high radio powers ($L_\nu(4.8 \text{ GHz}) \gtrsim 10^{25} \text{ W Hz}^{-1}$) and FIR luminosities $\nu L_\nu(60 \mu\text{m}) > 10^{10.7} L_\odot$. All but one of these quasars have large radio excesses with $u < -0.2$; Q0558-504 is the exception.

Q0558-504 (F05585-5026) is the only previously-known quasar with an intermediate radio excess. This object has $u = 0.39$. It is a luminous FIR and radio source with $L_\nu(4.8 \text{ GHz}) = 10^{25.0} \text{ W Hz}^{-1}$ and $\nu L_\nu(60 \mu\text{m}) = 10^{11.3} L_\odot$. It has a Narrow Line Seyfert 1 optical spectrum with bright and variable X-ray emission (Ballantyne, Iwasawa, & Fabian 2001).

4.8. Blazars

Blazars are common in the radio-excess sample; PKS 0235+164 (F02358+1623), PKS 0338-214 (F03384-2129), PKS 0420-014 (F04207-0127), PKS 0537-441 (F05373-4406), PKS 0735+17 (F07352+1749), PKS 0754+100 (F07543+1004), PKS 0829+046 (F08291+0439), OJ 287 (F08519+2017), PKS 1144-379 (F11445-3755), 3C 273 (F12265+0219), 3C 279 (F12535-0530), B2 1308+32 (F13080+3237), OQ 208 (F14047+2841), OQ 530 (F14180+5437), B2 1732+389 (F17326+3859), Q2005-489 (F20057-4858), BL Lac (F22006+4202), and 3C 446 (F22231-0512). These objects are BL Lacs, optically variable, flat radio spectrum quasars, or “transition objects” between traditional BL Lacs and (strong emission line) quasars. Many of the blazars have extremely high radio powers ($L_\nu(4.8 \text{ GHz}) > 10^{27} \text{ W Hz}^{-1}$) and FIR luminosities ($\nu L_\nu(60 \mu\text{m}) > 10^{13} L_\odot$) and are at relatively large redshifts ($z \gtrsim 0.9$). Blazars also occur in the sample at lower redshifts and powers, as low as $z \sim 0.05$ and $L_\nu(4.8 \text{ GHz}) \sim 10^{25} \text{ W Hz}^{-1}$. All the known blazars in the radio-excess sample have large radio excesses ($u < -0.2$), several with extreme values of $u \sim -1.0$. CAB comment that the blazars in their full sample all have $u < -0.15$ and spectral indices between 1.4 and 4.8 GHz of < 0.5 . This makes them flat spectrum objects with large radio excesses.

5. Discussion

5.1. Radio Properties

The radio-excess sample includes radio sources with a large range of physical sizes from $< 1 \text{ kpc}$ to $> 1 \text{ Mpc}$. Angular sizes or upper limits were measured from our *ATCA* observations for 51 radio-excess objects and physical sizes determined using the known redshifts. Sizes for a further 116 objects were obtained from the literature. Sizes for the radio sources and references are listed in Table 3. Of the 166 objects for which we have radio sizes, 102 are $\leq 15 \text{ kpc}$ in extent, implying that the radio source is embedded within the host galaxy in many cases. Of these, 7 are known blazars or BL Lac objects, leaving 95 compact non-blazar objects (57% of objects with measured sizes). Figures 4 and 5 show maps of the 17 sources observed with the *ATCA* that were resolved at 4.8 GHz and 8.6 GHz, respectively. The peak radio fluxes and contour levels are listed in Table 4. The radio contours are overlaid on DSS optical images. One of these objects (F13174-1651) is a pair of galaxies separated by 14 kpc. The eastern galaxy is resolved with a size of 5.5 kpc, the western galaxy is unresolved ($< 1 \text{ kpc}$). Three of the radio sources (F03079-3031, F08064-1018 and F20203-5733) are large radio galaxies with physical sizes of several hundred kpc. Only the core of F03079-3031 is shown in Fig.4 as the lobes were not detected. Another object (F22073-4044, redshift unknown) has lobes separated by $41''$ and may also be a large

radio galaxy. Five of the resolved sources have physical sizes less than 15 kpc; all except one of these (F05212-3630) appear from the DSS images to be similar in size to the optical sources. The remaining 7 objects have sizes of a few tens of kpc and are generally larger than the optical source.

Fig. 4.— **Please note: Figure 4 is provided separately in GIF format.** *ATCA* maps of radio-excess objects that are resolved at 4.8 GHz.

Fig. 5.— **Please note: Figure 5 is provided separately in GIF format.** *ATCA* maps of radio-excess objects that are resolved at 8.6 GHz.

Table 4. Contour levels for *ATCA* maps

FSC Name	ν (GHz)	Peak (mJy/beam)	Contour Levels (% of peak)
(1)	(2)	(3)	(4)
F00123-2356	4.79	3.1	20, 30, 40, 50, 70, 90
F01317-3644	4.79	31.4	7, 10, 30, 50, 70, 90
F03079-3031	4.79	25.5	5, 10, 20, 30, 50, 70, 80, 90
F03265-2852	4.79	265.2	1, 2, 5, 8, 10, 30, 50, 70, 80, 90
F04367-2726	8.64	8.4	10, 30, 50, 70, 80, 90
F05212-3630	4.79	2292.0	2, 5, 10, 30, 50, 70, 80, 90
F08064-1018	4.79	195.7	6, 10, 20, 30, 50, 70, 90
F10227-8251	4.79	11.6	10, 20, 30, 50, 70, 90
F13174-1651	4.79	17.2	4, 10, 20, 30, 50, 70, 90
F20203-5733	4.79	243.4	5, 10, 20, 30, 50, 70, 90
F21529-6955	4.79	809.0	6, 10, 14, 20, 30, 50, 70, 90
F22073-4044	4.79	111.6	15, 25, 50, 70, 90
F22521-3929	4.79	171.9	1, 2, 5, 10, 20, 30, 50, 70, 90
F22537-6512	8.64	50.2	5, 10, 20, 30, 50, 70, 80, 90
F23135-4745	8.64	142.8	1, 2, 5, 10, 20, 30, 50, 70, 90

Figure 6(a) shows the distribution of high frequency spectral indices for the radio-excess sources detected at 3 cm and 6 cm (8.6 GHz and 4.8 GHz, respectively) with the *ATCA*. Figure 6(b) shows the distribution of 6–20 cm spectral indices for those sources in the radio-excess sample with NVSS 20 cm flux measurements. To facilitate a comparison with CSS/GPS sources, non-blazar radio sources ≤ 15 kpc in extent are indicated separately in Figure 6. Most 3 – 6 cm spectral indices are in the range -1.5 – +1.0, with a modes of -0.9 for the whole radio-excess sample and -1.1 for the compact (< 15 kpc) objects. This is similar to other types of radio sources, including CSS/GPS sources (Stanghellini et al. 1998; Fanti et al. 2001). A large fraction of the compact objects (28 of 47 sources observed) have steep spectral indices ($\alpha_{3-6 \text{ cm}} < -0.5$). The 6–20 cm spectral indices cover a similar range, with a mode of -0.9 for both the compact objects and for the whole radio-excess sample. These steep spectral indices are similar to those observed in Seyfert radio sources, which have on average $\alpha_{6-20 \text{ cm}} \sim -0.7$ (Edelson 1987). The spectral index of F05265-4720 is highly inverted ($\alpha_{3-6 \text{ cm}} = 1.83$). This suggests either strong synchrotron self-absorption in a fairly homogeneous medium, or free-free absorption in a dense ionized medium. At the other extreme, F04023-1638 shows a very steep spectral index of -3.43. The spectral energy distribution of this source remains steep to 20 cm but with a shallower slope of -1.37. The cause of this extremely steep spectrum is not clear.

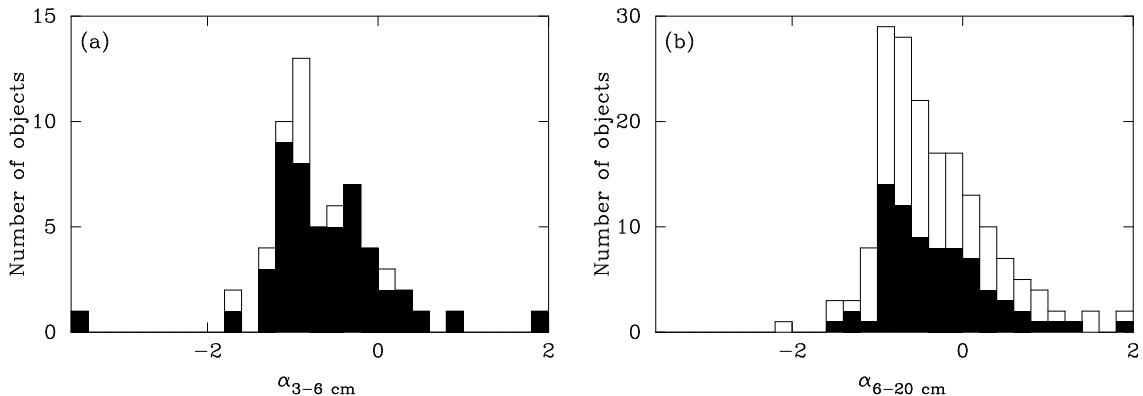


Fig. 6.— (a) Histogram of the radio spectral index, $\alpha_{3-6 \text{ cm}}$ ($S_\nu \propto \nu^\alpha$), between 3 and 6 cm for the radio-excess objects observed with the *ATCA*. (b) Histogram of the radio spectral index, $\alpha_{6-20 \text{ cm}}$, between 6 and 20 cm for the radio-excess objects with NVSS 20 cm flux densities. Objects with radio source extent ≤ 15 kpc, excluding known blazars, are shown filled, while the unfilled histogram shows the whole sample.

The compact radio-excess objects with steep spectral indices appear to be similar to CSS or GPS sources. This is consistent with the presence of known CSS/GPS sources in the sample (§4.6). CSS/GPS sources are powerful, optically-thin radio emitters that are also compact. They have been modeled using the same twin-jet models that apply to extended radio galaxies (e.g., Carvalho 1985; Begelman 1996). These models assume that twin jets of highly energetic and collimated relativistic plasma are expelled by the central engine into the surrounding interstellar medium of the host galaxy. A cocoon of shocked ISM material expands around the jets as the lobes develop. Hot spots (i.e., regions of high radio brightness) occur at the ends of the cocoon where the jet interacts directly with the ISM and where the cocoon expands fastest. The radio emission from the lobes and hot spots is optically thin at high frequencies, and dominates the total radio emission from the source. This results in the observed steep high frequency radio spectrum. The small size of CSS and GPS sources is argued to be due either to youth or confinement: they may be small because they are very young ($\lesssim 10^5$ yr) and will evolve into larger radio galaxies, or they may be small because they are confined by a dense surrounding medium that does not allow the radio lobes to expand.

Recent evidence has favored the youth model. The measurement of hotspot advance speeds of $\sim 0.2c$ (Owsianik & Conway 1998; Owsianik, Conway, & Polatidis 1999) show that at least some of the compact sources are expanding, and so are not permanently confined by the surrounding medium. Plausible evolutionary models linking CSS/GPS sources with extended radio galaxies (FR I/II) also provide support for the youth model (Carvalho 1985; Fanti et al. 1995; Readhead et al. 1996). The possibility that some CSS/GPS sources are confined by the host ISM has been investigated by numerical simulations and analytical models. Numerical simulations of a jet propagating in an ambient medium (De Young 1993) suggest that a typical CSS radio jet could be confined to a size < 10 kpc for $\sim 10^7$ years by an average ISM density of $\sim 1 - 10 \text{ cm}^{-3}$. This implies total gas masses in the host of $\sim 10^{11-12} M_{\odot}$. Similar results were obtained for a uniform density medium and a 2-phase medium consisting of dense clouds in a diffuse surrounding medium, with the same average density. A simple analytical model of jets interacting with dense clouds in the ISM (Carvalho 1994, 1998) has been used to show that some GPS sources could be confined to sizes less than a few hundred parsecs for 10^7 years by a cloud with central density $\sim 10^{3-4} \text{ cm}^{-3}$, assuming a total mass for the cloud of $10^{9-10} M_{\odot}$. Gas masses of $\sim 10^{10} M_{\odot}$ are known in some CSS/GPS sources; a mass of $\sim 3 \times 10^{10} M_{\odot}$ was inferred for PKS B1718-649 from H I absorption measurements (Véron-Cetty et al. 1995) and a mass of $\sim 7 \times 10^{10} M_{\odot}$ was derived from CO line emission for the source PKS 1345+12 (F13451+1232, present in our sample) (Evans et al. 1999). However, a recent study of 49 CSS/GPS sources found that the best-fit model to the observed H I column densities implied a gas mass of $\sim 10^8 M_{\odot}$ within a radius of 10 kpc (Pihlström, Conway, & Vermeulen 2003). This suggests that masses of $10^{10} M_{\odot}$ are not typical of CSS/GPS sources, so the ambient medium is not likely to be dense enough to confine the jet in most cases. Nevertheless, such high gas masses are typical in the central few hundred parsecs of luminous FIR galaxies (Mirabel & Sanders 1988; Sanders & Mirabel 1996). The FIR-luminous radio-excess objects could therefore have gas masses in the range $10^9-10^{10} M_{\odot}$. The masses and central densities of the host galaxies may be sufficient to confine the radio source. Measurements of CO line emission at millimeter wavelengths and H I (21 cm) absorption are needed to confirm this.

The radio powers of our compact steep-spectrum radio-excess objects are generally lower than well-known CSS and GPS sources. The objects in our radio-excess sample have radio powers as low as $10^{23} \text{ W Hz}^{-1}$, with a median of $\sim 10^{24.5} \text{ W Hz}^{-1}$ at 5 GHz. The median radio power of CSS and GPS sources at 5 GHz is $\sim 10^{27.6} \text{ W Hz}^{-1}$ (O’Dea 1998). This may be contrasted with the radio sources observed in Seyfert galaxies. These are also subgalactic (usually a few hundred parsecs; e.g., Schmitt et al. (2001); Ulvestad & Ho (2001)) and generally have optically thin spectra, but have a median power at 5 GHz of $10^{22} \text{ W Hz}^{-1}$ (Edelson 1987). The median redshift of the radio-excess sample is 0.063. This is significantly lower than the median redshift of CSS and GPS samples, which is $z = 0.91$, and considerably higher than the median redshift of the Seyfert galaxy sample, 0.0196. Thus a large part of the difference in radio powers may be attributable to the correlation between power and redshift for flux-limited samples. However, the radio jets observed in some Seyfert galaxies are likely to be intrinsically weaker than those in CSS/GPS sources and are subrelativistic (Bicknell 2002). It is possible that the radio-excess objects with intermediate radio powers have jet energy fluxes that fall in between those of Seyfert and CSS/GPS radio sources. Jet energy fluxes have been estimated from the luminosity of the [O III] λ 5007 Å emission line, based on shock-excitation models for the optical emission (Bicknell et al. 1998). A comparison of the [O III] λ 5007 Å luminosities of the radio-excess objects with those of Seyferts and CSS/GPS sources would reveal whether the radio-excess objects have jet energy fluxes intermediate between Seyferts and CSS/GPS sources.

It has been suggested that CSS/GPS sources may be precursors to FR I and II radio galaxies (e.g., Phillips & Mutel 1982; Carvalho 1985; O’Dea & Baum 1997). If CSS sources maintain a constant jet energy flux as their lobes expand into a uniform medium with radially declining density, the radio power will decrease due to the decrease in lobe pressure as the length increases (Begelman 1996). If powerful

CSS and GPS sources are the precursors of FR I and II radio galaxies, the relative numbers of CSS/GPS and extended radio sources demand that they must decrease in luminosity by factors of 10–100 as they expand (e.g., O’Dea & Baum 1997). More recently, however, it has been suggested that GPS sources (< 1 kpc in size) may increase in luminosity as they increase in size if they expand into a constant density medium (Snellen et al. 2000b). Clearly the circumnuclear environment of a young radio galaxy is complex and may well be clumpy on small scales, so these idealized models are only indicative. By fitting models to observed linear sizes and hot-spot advance speeds of GPS sources, Perucho & Martí (2002) conclude that GPS sources increase in luminosity with linear size up to 1 kpc, lending support to the suggestion. A source ~ 10 pc in size might be expected to increase in luminosity by a factor of ~ 20 as it expands to 1 kpc, assuming that the jet energy flux is constant and that the density of the surrounding medium is constant with radius. A radio-intermediate object with $L_{radio} = 10^{24}$ W Hz $^{-1}$ and size ~ 10 pc (in the “GPS phase”) could increase to $L_{radio} = 2 \times 10^{25}$ W Hz $^{-1}$ as it expanded to 1 kpc. It would then appear to be a radio-loud object (see Figure 2). As it expanded beyond 1 kpc, it would be expected to decrease in radio power again, and would possibly evolve into an FR I or FR II radio galaxy.

A turnover in the spectra of CSS and GPS sources is seen at frequencies $\lesssim 15$ GHz (O’Dea & Baum 1997) where the source becomes optically thick due to either synchrotron self-absorption or free-free absorption. The observed relationship between the turnover frequency and emission region size of CSS/GPS sources can be explained by either absorption model (O’Dea & Baum (1997) and Bicknell, Dopita, & O’Dea (1997), respectively). At frequencies around the turnover, the source appears to have a flat radio spectrum and below this frequency the spectrum is inverted. Compact objects in the radio-excess sample with flat or inverted spectral indices at centimeter wavelengths may be young radio sources observed near or below their spectral peak. These would be sources with turnover frequencies $\gtrsim 1$ GHz. The observed relation between turnover frequency and source size (O’Dea & Baum 1997) would then imply sizes $\lesssim 1$ kpc. This is credible because more compact objects (≤ 15 kpc, excluding known blazars) show α_{6-20cm} inverted (26% of those objects with measured α_{6-20cm} have $\alpha_{6-20cm} > 0$) than α_{3-6cm} (14% of those objects with measured α_{3-6cm} have $\alpha_{3-6cm} > 0$). Fewer objects show steep slopes between 6 cm and 20 cm than between 3 cm and 6 cm (51% with $\alpha_{6-20cm} > 0.5$ compared with 60% with $\alpha_{3-6cm} > 0.5$). These distributions of spectral slopes at low and high frequencies are consistent with the presence of GPS sources in the radio-excess population, which turn over at ~ 1 GHz.

Alternatively, the radio-excess objects with flat radio spectra may be core-dominated sources. The degree to which the emission is dominated by the optically thin lobes or the optically thick core is often used to infer whether the radio jet is aligned near to the line of sight. Generally, the closer the radio jet is to the line of sight the more core-dominated is the source and the flatter is its radio spectrum. Flat spectrum compact radio sources are usually associated with radio-loud quasars or BL Lac objects. The radio-FIR emission from blazars is believed to be synchrotron emission from relativistic plasma that is highly collimated and orientated close to the line of sight. The isotropic radio power of these objects is likely to over-estimate the true power because of relativistic beaming. In the absence of further information on the spectral energy distribution of the flat-spectrum, compact radio-excess sources, it may be possible to distinguish the blazars from CSS/GPS-like sources by measuring the polarization and rotation measure. Blazars are characterized by high levels of radio polarization ($\sim 2.5\%$; Iler et al. 1997) independent of observation frequency (Saikia & Salter 1988), while CSS/GPS sources show weak polarization ($\sim 0.2\%$ for GPS sources and up to 3% for CSS sources at 5 GHz) which varies with frequency, consistent with large observed rotation measures (O’Dea 1998).

Most objects were not observed to vary in radio flux. Twenty-six objects were measured with the ATCA on at least two occasions and were not found to vary significantly. This is similar to GPS sources, which are the least variable of radio sources (O’Dea 1998). Two of the radio-intermediate objects observed with the ATCA were observed to vary in flux density. F01264-5705, was found to increase in flux density by a factor of 1.85 at 8.6 GHz between observations separated by 18 months. F01264-5705 is a compact

radio source with a highly inverted radio spectrum. F11445-3755 was observed to increase in flux density by factors of 1.2 at 4.8 GHz and 1.4 at 8.6 GHz within one month. This object is a known blazar (PKS 1144-379). However, the general lack of variability is more consistent with the radio-excess objects being similar to CSS/GPS sources, rather than blazars.

5.2. Far-Infrared Properties

The *IRAS* 25 μm to 60 μm color, $\log [S_\nu(60 \mu\text{m})/S_\nu(25 \mu\text{m})]$, is a useful parameter distinguishing starburst galaxies from AGN (de Grijp, Miley, & Lub 1987; Low et al. 1988; Sanders et al. 1988a; de Grijp et al. 1992). Starbursts tend to have cool 25–60 μm color temperatures with $\log [S_\nu(60 \mu\text{m})/S_\nu(25 \mu\text{m})] > 0.57$ because of their extended star and gas distributions, while the central engines in AGN heat the large amounts of nearby dust to warmer temperatures so $0.0 < \log [S_\nu(60 \mu\text{m})/S_\nu(25 \mu\text{m})] < 0.57$ (Low et al. 1988). It is therefore of interest to compare $\log [S_\nu(60 \mu\text{m})/S_\nu(25 \mu\text{m})]$ with the radio excess for each object, which we also use to infer the presence of an AGN. Figure 7(a) shows this comparison for all objects in the full sample with 25 μm *IRAS* detections.

Figure 7(b) shows the colors and radio excesses of the comparison objects (see Table 2). As is well known, starburst galaxies are radio quiet and have cool far-infrared colors. In general, the Seyfert galaxies in Figure 7(b) have warm far-infrared colors and small radio excesses. The classical radio-loud galaxies and quasars in Figure 7(b) have large radio excesses and almost exclusively have warm far-infrared colors. The radio-quiet quasars in Figure 7(b) have low radio excesses that are similar to those of the starburst and Seyfert galaxies, but the far-infrared colors of the radio-quiet quasars are at least as warm as those of the radio-loud galaxies and quasars.

Our radio-excess sample includes objects with both cool and warm far-infrared colors, suggesting that the sample may contain objects powered by both starbursts and AGN. It will be of interest to establish whether the radio-intermediate objects with cool far-infrared colors do indeed have optical spectra indicative of starbursts, whether these are objects in which the AGN is so heavily embedded that the emission is optically thick at far-infrared wavelengths, or whether these objects lack a significant dust mass in close proximity to the AGN so exhibit only cool dust emission.

There is a tendency in Figure 7(a) for objects with warmer far-infrared colors to also have larger radio excesses (small u values). However, comparison of Figures 7(a) and 7(b) shows that the lower bound of this distribution is due largely to the absence of radio-quiet quasars in our full sample. This exclusion is traced to the relatively high radio flux limits of both the PMN and Greenbank 4.8 GHz surveys: most radio-quiet quasars fall below the radio flux limits of both our sample and that of CAB.

Few objects appear in Figure 7(a) that are both radio loud and have cool far-infrared colors. This supports the association of extreme excess radio emission with an AGN.

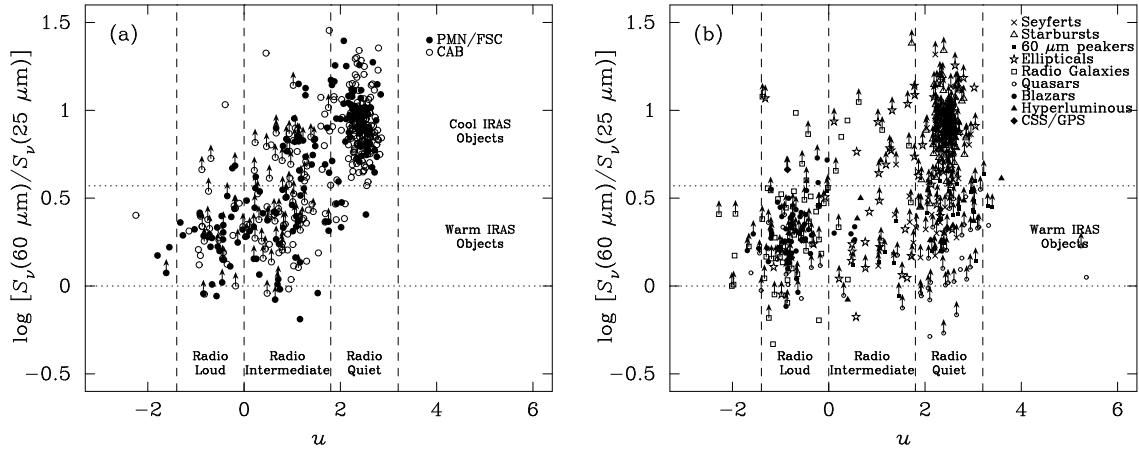


Fig. 7.— (a) FIR color, $\log [S_\nu(60 \mu\text{m})/S_\nu(25 \mu\text{m})]$, vs radio/FIR flux ratio, $u = \log [S_\nu(60 \mu\text{m})/S_\nu(4.8 \text{ GHz})]$, for the full sample. The vertical dashed lines define regions occupied by radio-quiet, radio-intermediate, and radio-loud objects. The horizontal dotted lines define regions occupied by “warm” and “cool” *IRAS* galaxies (de Grijp et al. 1987). (b) FIR color, $\log [S_\nu(60 \mu\text{m})/S_\nu(25 \mu\text{m})]$, vs radio/FIR flux ratio, u , for the comparison objects (see Table 2). The marked regions are the same as for (a).

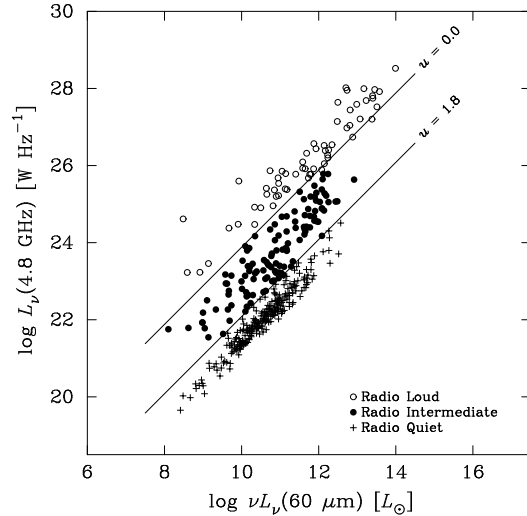


Fig. 8.— Radio/FIR luminosity diagram for the full PMN/FSC and CAB samples showing radio-loud, radio-intermediate, and radio-quiet objects with different symbols. Lines corresponding to $u = 1.8$ and $u = 0.0$ at zero redshift are labelled.

Figure 8 reproduces the radio/FIR luminosity diagram for the full PMN/FSC and CAB samples segregated according to u value; radio-quiet objects ($u \geq 1.8$), radio-intermediate objects ($0.0 < u < 1.8$), and radio-loud objects ($u \leq 0.0$) are plotted with different symbols. These objects are shown with the same symbols in far-infrared two-color diagrams in Figure 9, which indicates the different color distributions of radio-quiet, radio-intermediate and radio-loud objects. The distribution of objects in Figure 9 is bounded by a starburst line, a reddening line, and an extreme mixing line, as explained by Dopita et al. (1998). These loci are shown separately for clarity in Figure 10. The starburst line was derived from the observed colors of starburst galaxies (Dopita et al. 1998). Starburst and star-forming galaxies exhibit a range of $\log [S_\nu(25 \mu\text{m})/S_\nu(12 \mu\text{m})]$ and $\log [S_\nu(60 \mu\text{m})/S_\nu(25 \mu\text{m})]$ ratios due to a range of different dust temperatures. Warmer star-forming galaxies have higher $\log [S_\nu(25 \mu\text{m})/S_\nu(12 \mu\text{m})]$ and lower $\log [S_\nu(60 \mu\text{m})/S_\nu(25 \mu\text{m})]$ ratios due to the shift of the blackbody peak to shorter wavelengths (i.e. towards $25 \mu\text{m}$). A pure Seyfert 1 nucleus is assumed to have $\log [S_\nu(60 \mu\text{m})/S_\nu(25 \mu\text{m})] = -0.03$ and $\log [S_\nu(25 \mu\text{m})/S_\nu(12 \mu\text{m})] = 0.22$ (Dopita et al. 1998). The extreme mixing line is determined by mixing the unreddened Seyfert 1 spectrum with increasing fractions of “cool” starburst spectrum having intrinsic colors of $\log [S_\nu(60 \mu\text{m})/S_\nu(25 \mu\text{m})] = 0.0$ and $\log [S_\nu(25 \mu\text{m})/S_\nu(12 \mu\text{m})] = 1.09$. The reddening law is taken from (Dopita et al. 1998). For each object, the relative contributions of starburst and AGN components, combined with the degree of reddening, define its place in the color-color diagram.

The FIR color-color diagram shows differences in the colors of objects with different degrees of radio excess (Fig. 9). The radio-quiet objects in our sample show similar FIR color distributions to those seen in normal and starburst galaxies (Rush, Malkan, & Spinoglio 1993). The high FIR luminosity ($> 10^{11} L_\odot$) radio-quiet objects extend over the full range of starburst colors (Fig. 9(b)), with a few objects being distributed along the Seyfert 1 galaxy reddening line. The low FIR luminosity ($< 10^{11} L_\odot$) radio-quiet objects (Fig. 9(c)) cluster predominantly near one end of the starburst distribution. This is the region occupied by cool starburst galaxies in which $11.3 \mu\text{m}$ PAH emission dominates the $S_\nu(25 \mu\text{m})/S_\nu(12 \mu\text{m})$ color (Dopita et al. 1998). The high FIR luminosity objects may contain hotter dust or the destruction of PAH molecules may be more complete in the high FIR luminosity objects, possibly due to the greater prominence of radio-quiet AGN. Radio-loud objects with both high and low FIR luminosities cluster around the unreddened Seyfert 1 region in Figure 9. These objects are clearly AGN-dominated with $12 \mu\text{m}$ optical depths generally below 2.0. In contrast, the radio-intermediate objects span the color range between the starburst sequence and the unreddened Seyfert 1 region in this diagram. The high FIR luminosity radio-intermediate objects are confined to the Seyfert 1 galaxy reddening line with $12 \mu\text{m}$ optical depths up to ~ 4.0 (Fig. 9(b)). We infer from this that at high FIR luminosities radio-intermediate objects are more heavily obscured than are the radio-loud objects, which have more extreme radio excesses. The high FIR luminosity radio-intermediate objects occupy the same region of the FIR color-color diagram occupied by hidden broad-line region (BLR) objects in which the BLR is revealed by either spectropolarimetry observations (Heisler et al. 1997) or by near-infrared emission-line spectroscopy (Veilleux et al. 1997). This similarity suggests that hidden BLRs may be detectable by these techniques in several of the high FIR luminosity radio-intermediate objects. The low FIR luminosity radio-intermediate objects extend along the mixing line between the “blue” end of the starburst sequence and the unreddened Seyfert 1 region. Approximately half of the low FIR luminosity radio-intermediate objects have FIR colors that are indistinguishable from those of starburst galaxies. These differences in the FIR colors of the high and low FIR luminosity radio-intermediate objects suggest that these objects may have fundamentally different physical natures.

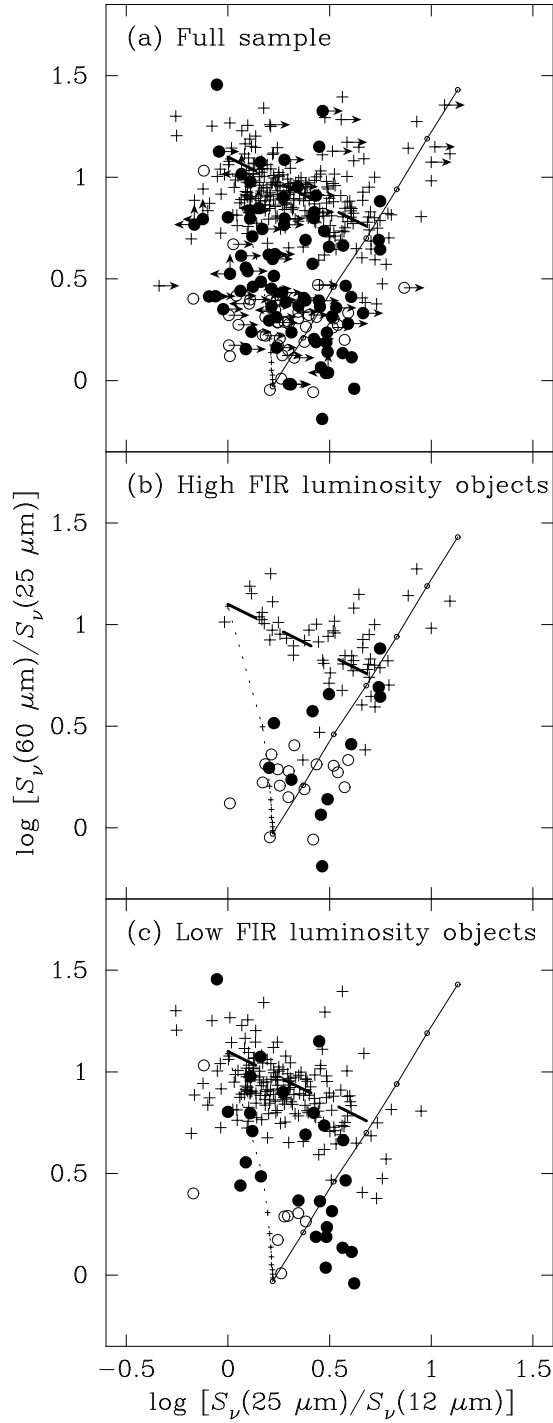


Fig. 9.— Far-infrared color-color diagram showing the positions of objects with different radio excesses (as in Fig. 8). The top panel shows all PMN/FSC and CAB objects, the middle panel shows only high FIR luminosity objects with $\nu L_\nu(60 \mu\text{m}) > 10^{11} L_\odot$ and detected at all three FIR wavelengths, and the bottom panel shows only low FIR luminosity objects with $\nu L_\nu(60 \mu\text{m}) < 10^{11} L_\odot$ and detected at all three FIR wavelengths. The starburst, mixing, and reddening lines are as shown in Fig. 10. The symbols used are as shown in Fig. 8.

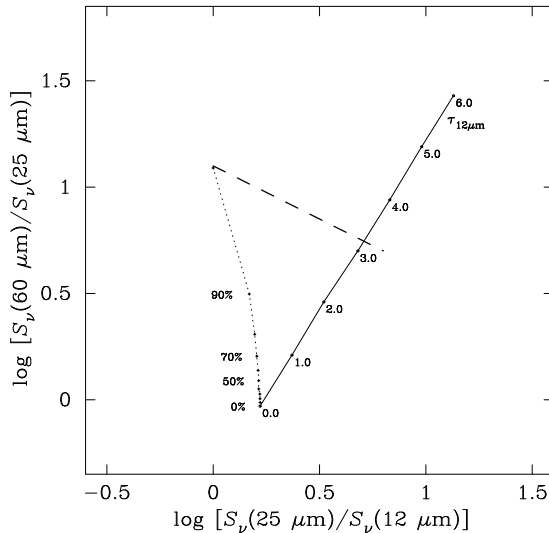


Fig. 10.— Far-infrared color-color diagram showing the mean locus of starburst galaxies (*dashed line*), an extreme mixing line between a pure Seyfert 1 spectrum and a starburst spectrum (*dotted line*), and the reddening line determined by obscuring a Seyfert 1 spectrum with the 12 μm optical depths that are indicated (*solid line*).

5.3. Optical Properties

SuperCosmos optical photographic photometry¹⁰ has been assembled for most objects south of declination $+2.5^\circ$ in the PMN/FSC and CAB samples. The R magnitudes are accurate to only ~ 0.5 mag (Hambly, Irwin, & MacGillivray 2001). However, this is sufficient to derive indicative total absolute magnitudes, $M(R)$. The distribution of $M(R)$ is shown in Fig. 11(a) for the radio-excess objects with SuperCosmos R magnitudes and known redshifts. The optical counterparts to these radio-excess objects are all high luminosity galaxies with $M(R)$ comparable to or brighter than that of an L^* galaxy (indicated by a dotted line in Fig. 11). This is consistent with other evidence that radio activity is associated with massive host galaxies (Dunlop 2001). There is a suggestion in Fig. 11(a) that the high FIR luminosity objects also have higher optical luminosities. Calibration uncertainties in the photographic photometry are such that CCD photometry will be required to verify this result.

The magnitude distribution for the optical counterparts of the radio-quiet objects is shown in Figure 11(b). The peak of the radio-quiet objects is about 1.5 magnitudes fainter than that of the radio-excess objects. The distribution of radio-quiet objects also extends to fainter optical magnitudes. This further supports the suggestion that the radio activity is associated with massive, luminous galaxies, although more accurate photometry is required to confirm this result.

6. Conclusions

The *IRAS* FSC 60 μm data have been cross-correlated with the PMN 5 GHz catalog to identify objects that emit significantly at both radio and FIR wavelengths. A significant population of radio-excess objects has been found that lies above the radio-quiet radio/FIR correlation. We find that the fraction of radio-intermediate objects in our sample is much larger than has been found by previous authors,

¹⁰<http://www-wfau.roe.ac.uk/sss/>

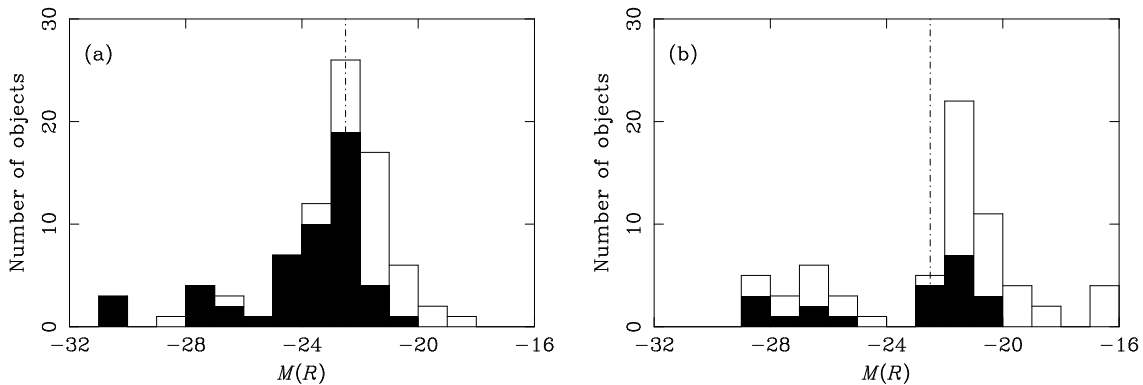


Fig. 11.— Distribution of absolute R magnitude for radio-excess objects (a) and radio-quiet objects (b) south of declination $+2.5^\circ$ based on SuperCosmos photographic photometry. Filled regions indicate high FIR luminosity ($\nu L_\nu(60 \mu\text{m}) > 10^{11} L_\odot$) objects. Unfilled regions indicate low FIR luminosity ($\nu L_\nu(60 \mu\text{m}) < 10^{11} L_\odot$) objects. The dotted line corresponds to an L^* galaxy with $M(R) = -22.5$ mag (Blanton et al. 2001).

especially at high FIR luminosities. This is because we have probed to lower *IRAS* flux densities. Future surveys by SIRTf are expected to discover more of these objects. The radio-excess objects appear to be uniformly distributed in the radio/FIR luminosity diagram between the radio-quiet sequence and the extreme radio-loud limit. There is no evidence for a separate radio-loud sequence. The apparent division of AGN into distinct radio-quiet and radio-loud classes appears to be due to the high flux density limits of previous radio surveys. This also affects our sample in that objects with small radio excesses and faint $60 \mu\text{m}$ flux densities are excluded because they fall below the PMN flux limit.

Many of the radio-excess objects have optically thin radio emission on scales ≤ 15 kpc, likely to be smaller than the host galaxy. These properties are similar to CSS/GPS sources, but the radio-excess objects have lower radio powers that are closer on average to those of Seyfert radio sources than CSS/GPS sources. Higher resolution radio data are required to determine the morphologies and sizes of the radio-excess sources. More spectral energy distribution data are also needed to determine if the spectra of the radio-excess objects turn over at GHz frequencies. This will allow us to more confidently test whether the radio-excess objects are low power CSS/GPS sources, with the same physical processes driving the radio emission as in these objects.

Differences between the FIR colors of the radio-excess objects with low and high FIR luminosities suggest they may be different types of objects. Some low far-infrared luminosity radio-excess objects appear to derive a dominant fraction of their far-infrared emission from star formation, despite the dominance of the AGN at radio wavelengths. Amongst the high FIR luminosity objects, we find that those with higher radio excesses tend to have FIR colors typical of unobscured Seyfert 1 galaxies, and objects with smaller radio excesses have colors indicating higher obscuration. If the radio power, and hence the radio excess, increases with age this may suggest that younger sources are more obscured than older sources. Our radio-excess sample contains high FIR luminosity objects over the full range of radio excesses. Well-studied interacting Seyfert galaxies with compact radio emission are present among the radio-quiet and radio-intermediate members of the sample. At high FIR luminosities, these are caused by the mergers of large dusty spiral galaxies, such as the Superantennae and Mrk 463. They contrast with the powerful isolated radio galaxies, such as 3C 195, which have large radio excesses and may be associated with the infall of a smaller dusty companion into an elliptical galaxy. These powerful radio sources may also be in a more advanced merger state than the less luminous radio sources that still exhibit two separate optical nuclei. This suggests that the merging activity may be associated with the

development of the radio source. It is clearly of interest to obtain higher quality optical images of the radio-excess galaxies. This would reveal the true morphologies of the host galaxies, and allow us to determine what fraction of the radio-excess objects are interacting and whether they are in an early or late merger stage.

The properties of many of the radio-excess objects are consistent with an evolutionary picture in which young radio sources are emerging from a dusty nucleus, and increasing in radio power as they evolve. Objects with $\nu L_\nu(60 \mu\text{m}) \gtrsim 10^{11} L_\odot$ are classified as luminous and ultra-luminous infrared galaxies. Such high FIR luminosities can be powered by merging activity between galaxies. It is known from observations (Sanders et al. 1986, 1988c) and numerical simulations (Barnes & Hernquist 1996) that tidal interactions between galaxies can funnel gas towards the nucleus, which may trigger bursts of star formation. Interactions and mergers have also been associated with the fuelling of AGN activity and with the generation of powerful radio emission (Heckman et al. 1986), although strong tidal interaction does not necessarily produce a radio-loud AGN (Smith & Kassim 1993). If the radio-excess objects are low-power CSS/GPS sources, they are likely to be young radio sources, triggered by tidal interactions that are also responsible for the high FIR luminosities. In this case, even if the radio-excess sources were initially in a “GPS phase”, increasing in radio power as they evolved, they will eventually fade as the radio lobes expand. It is possible that they may fade to radio-quiet objects or weak FR I’s.

Alternatively, it is possible that the radio sources may be confined by the high gas density in the nuclear region, FIR-luminous galaxies have higher gas masses than observed in CSS/GPS sources, which may be sufficient to confine the radio jets. The weaker radio powers of the radio-excess objects may be due to intrinsically weaker radio jets which would be easier to confine than powerful CSS/GPS sources. Several observational tests may be made to determine whether the FIR luminous radio-excess objects are likely to be young or confined. Observations to detect H I absorption or CO emission would provide estimates of the gas masses in the hosts, which could indicate whether confinement is possible. A study of the radio spectral energy distributions of the objects may enable an estimate of the age of the emitting electrons via synchrotron cooling. Measurement of the [O III] λ 5007 Å luminosities will allow an estimate of the jet energy fluxes, which may be compared with those of Seyfert radio sources and CSS/GPS sources.

Optical spectroscopy will also be useful to confirm the presence of an AGN and to assess how dominant the AGN is in the optical regime. Furthermore, if these really are CSS/GPS sources, it may be useful to distinguish the quasars from the narrow-line objects, as it has been suggested that these two classes of CSS/GPS sources are physically different types of object that share only a similar spectral shape (Snellen, Schilizzi, & van Langevelde 2000a). The FIR colors of the high luminosity objects suggest large obscurations even at FIR wavelengths; optical spectra may be used to determine the optical extinction which should be high. The high FIR luminosities of these objects may indicate merging activity, which would be expected to be accompanied by starburst activity. Two of the well-studied CSS sources in the sample, 3C 459 and 3C 48, show optical absorption spectra and blue continua that are indicative of a young stellar population. This lends support to the idea that the radio sources are young, rather than pressure-confined. Similarly, optical spectra of the radio-excess objects may be used to determine if there has been recent star formation and estimate the age of the dominant stellar population.

We thank Lisa Kewley for help at an early stage of this research and Geoff Bicknell for useful discussions. The assistance of the duty astronomers at the Australia Telescope Compact Array is much appreciated. Drake is the holder of an Australian Postgraduate Research Award and a Duffield Scholarship. MD wishes to acknowledge the support of the Australian National University and the Australian Research Council (ARC) through his ARC Australian Federation Fellowship, and also under ARC Discovery project DP0208445. The Australia Telescope is funded by the Commonwealth of Australia for operation as a National Facility managed by CSIRO. This research has made use of the NASA/IPAC Extragalactic Database (NED) which is operated by the Jet Propulsion Laboratory, California Institute

of Technology, under contract with the National Aeronautics and Space Administration. The Digitized Sky Surveys were produced at the Space Telescope Science Institute under U.S. Government grant NAG W-2166. The images of these surveys are based on photographic data obtained using the Oschin Schmidt Telescope on Palomar Mountain and the UK Schmidt Telescope. The plates were processed into the present compressed digital form with the permission of these institutions. IRAF is distributed by the National Optical Astronomy Observatories, which are operated by the Association of Universities for Research in Astronomy, Inc., under cooperative agreement with the National Science Foundation.

REFERENCES

- Altschuler, D. R., Gurvits, L. I., Alef, W., Dennison, B., Graham, D., Trotter, A. S., & Carson, J. E. 1995, *A&AS*, 114, 197
- Antonucci, R. R. J., & Ulvestad, J. S. 1985, *ApJ*, 294, 158
- Armus, L., Heckman, T. M., & Miley, G. K. 1989, *ApJ*, 347, 727
- Bajaja, E., Hummel, E., Wielebinski, R., & Dettmar, R.-J. 1988, *A&A*, 202, 35
- Ballantyne, D. R., Iwasawa, K., & Fabian, A. C. 2001, *MNRAS*, 323, 506
- Barnes, J. E., & Hernquist, L. 1996, *ApJ*, 471, 115
- Barvainis, R., & Antonucci, R. 1989, *ApJS*, 70, 257
- Barvainis, R., & Lonsdale, C. 1997, *AJ*, 113, 144
- Baum, S. A., O’Dea, C. P., Dallacassa, D., de Bruyn, A. G., & Pedlar, A. 1993, *ApJ*, 419, 553
- Becker, R. H., White, R. L., & Helfand, D. J. 1995, *ApJ*, 450, 559
- Begelman, M. C. 1996, in *Cygnus A: A Study of a Radio Galaxy*, ed. C. L. Carilli, & D. A. Harris (Cambridge: Cambridge University Press), 209
- Bennett, A. S. 1963, *MmRAS*, 68, 163
- Bicknell, G. V. 2002, *NewAR*, 46, 365
- Bicknell, G. V., Dopita, M. A., & O’Dea, C. P. 1997, *ApJ*, 485, 112
- Bicknell, G. V., Dopita, M. A., Tsvetanov, Z. I., & Sutherland, R. S. 1998, *ApJ*, 495, 680
- Black, A. R. S., Baum, S. A., Leahy, J. P., Perley, R. A., Riley, J. M., & Scheuer, P. A. G. 1992, *MNRAS*, 256, 186
- Blanton, M. R., et al. 2001, *AJ*, 121, 2358
- Blundell, K. M., & Lacy, M. 1995, *MNRAS*, 274, L9
- Borne, K. D., Bushouse, H., Lucas, R. A., & Colina, L. 2000, *ApJ*, 529, L77
- Borson, T. A., & Oke, J. B. 1984, *ApJ*, 281, 535
- Bridle, A. H., Fomalont, E. B., & Cornwell, T. J. 1981, *AJ*, 86, 1294
- Broadhurst, T., & Lehar, J. 1995, *ApJ*, 450, L41
- Browne, I. W. A., Wilkinson, P. N., Patnaik, A. R., & Wrobel, J. M. 1998, *MNRAS*, 293, 257
- Capetti, A., de Ruiter, H. R., Fanti, R., Morganti, R., Parma, P., & Ulrich, M.-H. 2000, *A&A*, 362, 871
- Carvalho, J. C. 1985, *MNRAS*, 215, 463
- Carvalho, J. C. 1994, *A&A*, 292, 329
- Carvalho, J. C. 1998, *A&A*, 329, 845
- Cassaró, P., Stanghellini, C., Bondi, M., Dallacasa, D., della Ceca, R., & Zappalà, R. A. 1999, *A&AS*, 139, 601
- Colbert, J. W., Mulchaey, J. S., & Zabludoff, A. I. 2001, *AJ*, 121, 808
- Colina, L., Sparks, W. B., & Macchetto, F. 1991, *ApJ*, 370, 102
- Condon, J. J., Anderson, E., & Broderick, J. J. 1995, *AJ*, 109, 2318 (CAB)
- Condon, J. J., Anderson, M. L., & Helou, G. 1991a, *ApJ*, 376, 95
- Condon, J. J., & Broderick, J. J. 1986, *AJ*, 92, 94
- Condon, J. J., & Broderick, J. J. 1988, *AJ*, 96, 30
- Condon, J. J., & Broderick, J. J. 1991, *AJ*, 102, 1663
- Condon, J. J., Condon, M. A., Gisler, G., & Puschell, J. J. 1982, *ApJ*, 252, 102
- Condon, J. J., Cotton, W. D., Greisen, E. W., Yin, Q. F., Perley, R. A., Taylor, G. B., & Broderick, J. J. 1998, *AJ*, 115, 1693
- Condon, J. J., Frayer, D. T., & Broderick, J. J. 1991b, *AJ*, 101, 362
- Corbett, E. A., et al. 2002, *ApJ*, 564, 650

- Cram, L. E., North, A., & Savage, A. 1992, *MNRAS*, 257, 602
- Crawford, T., Marr, J., Partridge, B., & Strauss, M. A. 1996, *ApJ*, 460, 225
- de Grijp, M. H. K., Miley, G. K., & Lub, J. 1987, *A&AS*, 70, 95
- de Grijp, M. H. K., Keel, W. C., Miley, G. K., Goudfrooij, P., & Lub, J. 1992, *A&AS*, 96, 389
- de Jong, T., Klein, U., Wielebinski, R., & Wunderlich, E. 1985, *A&A*, 147, L6
- Dey, A., & van Breugel, W. 1994, in *Mass-Transfer Induced Activity in Galaxies*, ed. I. Shlosman (Cambridge: Cambridge University Press), 263
- De Young, D. S. 1993, *ApJ*, 402, 95
- Dickey, J. M., & Salpeter, E. E. 1984, *ApJ*, 284, 461
- Dopita, M. A., Heisler, C. A., Lumsden, S., & Bailey, J. 1998, *ApJ*, 498, 570
- Dopita, M. A., Koratkar, A. P., Allen, M. G., Tsvetanov, Z. I., Ford, H. C., Bicknell, G. V., & Sutherland, R. S. 1997, *ApJ*, 490, 202
- Dunlop, J. S. 2001, in *QSO hosts and their environments*, ed. I. Márquez, J. Masegosa, A. Del Olmo, L. Lara, E. García, & J. Molina (Dordrecht: Kluwer Academic / Plenum Publishers), 3
- Edelson, R. A. 1987, *ApJ*, 313, 651
- Edelson, R. A., Malkan, M. A., & Rieke, G. H. 1987, *ApJ*, 321, 233
- Elvis, M., et al. 1994, *ApJS*, 95, 1
- Evans, A. S., Kim, D. C., Mazzarella, J. M., Scoville, N. Z., & Sanders, D. B. 1999, *ApJ*, 521, L107
- Falcke, H., Wilson, A. S., & Simpson, C. 1998, *ApJ*, 502, 199
- Fanaroff, B. L., & Riley, J. M. 1974, *MNRAS*, 167, 31
- Fanti, C., Fanti, R., Dallacasa, D., Schilizzi, R. T., Spencer, R. E., & Stanghellini, C. 1995, *A&A*, 302, 317
- Fanti, C., Fanti, R., de Ruiter, H. R., & Parma, P. 1986, *A&AS*, 65, 145
- Fanti, C., Fanti, R., de Ruiter, H. R., & Parma, P. 1987, *A&AS*, 69, 57
- Fanti, R., Fanti, C., Schilizzi, R., Spencer, R., Redong, N., Parma, P., van Breugel, W., & Venturi, T. 1990, *A&A*, 231, 333
- Fanti, C., Pozzi, F., Dallacasa, D., Fanti, R., Gregorini, L., Stanghellini, C., & Vigotti, M. 2001, *A&A*, 369, 380
- Fosbury, R. A. E., Morganti, R., Wilson, W., Ekers, R. D., di Serego Alighieri, S., & Tadhunter, C. N. 1998, *MNRAS*, 296, 701
- Gabuzda, D. C., & Cawthorne, T. V. 2000, *MNRAS*, 319, 1056
- Gelderman, R., & Whittle, M. 1994, *ApJS*, 91, 491
- Ghosh, K. K., & Soundararajaperumal, S. 1995, *ApJS*, 100, 37
- Gilmore, G., & Shaw, M. A. 1986, *Nature*, 321, 750
- Golombek, D., Miley, G. K., & Neugebauer, G. 1988, *AJ*, 95, 26
- Gregory, P. C., & Condon, J. J. 1991, *ApJS*, 75, 1011
- Griffith, M. R., & Wright, A. E. 1993, *AJ*, 105, 1666
- Griffith, M. R., Wright, A. E., Burke, B. F., & Ekers, R. D. 1994, *ApJS*, 90, 179
- Griffith, M. R., Wright, A. E., Burke, B. F., & Ekers, R. D. 1995, *ApJS*, 97, 347
- Hambly, N. C., Irwin, M. J., & MacGillivray, H. T. 2001, *MNRAS*, 326, 1295
- Hamuy, M., Walker, A. R., Suntzeff, N. B., Gigoux, P., Heathcote, S. R., & Phillips, M. M. 1992, *PASP*, 104, 533
- Hamuy, M., Suntzeff, N. B., Heathcote, S. R., Walker, A. R., Gigoux, P., & Phillips, M. M. 1994, *PASP*, 106, 566
- Heckman, T. M. 1980, *A&A*, 87, 152
- Heckman, T. M., Smith, E. P., Baum, S. A., van Breugel, W. J. M., Miley, G. K., Illingworth, G. D., Bothun, G. D., & Balick, B. 1986, *ApJ*, 311, 526
- Heisler, C. A., Lumsden, S. L., & Bailey, J. A. 1997, *Nature*, 385, 700
- Helou, G., Soifer, B. T., & Rowan-Robinson, M. 1985, *ApJ*, 298, L7
- Hutchings, J. B., Neff, S. G., Weadock, J., Roberts, L., Ryneveld, S., & Gower, A. C. 1994, *AJ*, 107, 471
- Iler, A. L., Schachter, J. F., & Birkinshaw, M. 1997, *ApJ*, 486, 117
- Impey, C. D., & Neugebauer, G. 1988, *AJ*, 95, 307
- Jauncey, D. L., Savage, A., Morabito, D. D., Preston, R. A., Nicolson, G. D., & Tzioumis, A. K. 1989, *AJ*, 98, 54
- Kellerman, K. I., Sramek, R., Schmidt, M., Shaffer, D. B., & Green, R. 1989, *AJ*, 98, 1195
- Kinney, A. L., Bohlin, R. C., Calzetti, D., Panagia, N., & Wyse, R. F. G. 1993, *ApJS*, 86, 5
- Knapp, G. R., Guhathakurta, P., Kim, D.-W., & Jura, M. A. 1989, *ApJS*, 70, 329
- Knapp, G. R., Bies, W. E., & van Gorkom, J. H. 1990, *AJ*, 99, 476
- Kuhr, H., Witzel, A., Pauliny-Toth, I. I. K., & Nauber, U. 1981, *A&AS*, 45, 367

- Landau, R., et al. 1986, ApJ, 308, 78
- Leahy, J. P., Black, A. R. S., Dennett-Thorpe, J., Hardcastle, M. J., Komissarov, S., Perley, R. A., Riley, J. M., & Scheuer, P. A. G. 1997, MNRAS, 291, 20
- Lister, M. L., Kellermann, K. I., Vermeulen, R. C., Cohen, M. H., Zensus, J. A., & Ros, E. 2003, ApJ, 584, 135
- Low, F. J., Huchra, J. P., Kleinmann, S. G., & Cutri, R. M. 1988, ApJ, 327, L41
- Magain, P., Surdej, J., Swings, J.-P., Borgeest, U., & Kayser, R. 1988, Nature, 334, 325
- Martel, A., et al. 1999, ApJS, 122, 81
- Mauch, T., Murphy, T., Buttery, H. J., Curran, J., Hunstead, R. W., Piestrzynski, B., Robertson, J. G., & Sadler, E. M. 2003, MNRAS, in press (astro-ph/0303188)
- Mazzarella, J. M., & Boroson, T. A. 1993, ApJS, 85, 27
- Mazzarella, J. M., Soifer, B. T., Graham, J. R., Neugebauer, G., Matthews, K., & Gaume, R. A. 1991, AJ, 102, 1241
- Miller, J. S. 1981, PASP, 93, 681
- Miller, L., Peacock, J. A., & Mead, A. R. G. 1990, MNRAS, 244, 207
- Mirabel, I. F. 1989, ApJ, 340, L13
- Mirabel, I. F., Lutz, D., & Maza, J. 1991, A&A, 243, 367
- Mirabel, I. F., & Sanders, D. B. 1988, ApJ, 335, 104
- Morganti, R., Killeen, N. E. B., & Tadhunter, C. N. 1993, MNRAS, 263, 1023
- Morganti, R., Oosterloo, T., Tadhunter, C. N., Aiudi, R., Jones, P., & Villar-Martin, M. 1999a, A&AS, 140, 355
- Morganti, R., Tsvetanov, Z. I., Gallimore, J., & Allen, M. G. 1999b, A&AS, 137, 457
- Moshir, M., et al. 1992, Explanatory Supplement to the *IRAS* Faint Source Survey, Version 2, JPL D-10015 8/92 (Pasadena:JPL)
- Mundell, C. G., Wilson, A. S., Ulvestad, J. S., & Roy, A. L. 2000, ApJ, 529, 816
- Norris, R. P., Kesteven, M. J., Troupe, E., & Allen, D. A. 1988, MNRAS, 234, 51
- O’Dea, C. P. 1990, MNRAS, 245, 20
- O’Dea, C. P. 1998, PASP, 110, 493
- O’Dea, C. P., Barvainis, R., & Challis, P. M. 1988, AJ, 96, 435
- O’Dea, C. P., & Baum, S. A. 1997, AJ, 113, 148
- O’Dea, C. P., Baum, S. A., Stanghellini, C., Morris, G. B., Patnaik, A. R., & Gopal-Krishna 1990, A&AS, 84, 549
- O’Dea, C. P., Baum, S. A., & Stanghellini, C. 1991, ApJ, 380, 66
- O’Dea, C. P., Stanghellini, C., Baum, S. A., & Charlot, S. 1996, ApJ, 470, 806
- Oke, J. B., & Gunn, J. E. 1983, ApJ, 266, 713
- Owen, F. N., Eilek, J. A., & Kassim, N. E. 2000, ApJ, 54, 611
- Owen, F. N., Spanger, S. R., & Cotton, W. D. 1980, AJ, 85, 351
- Owsianik, I., & Conway, J. E. 1998, A&A, 337, 69
- Owsianik, I., Conway, J. E., & Polatidis, A. G. 1999, NewAR, 43, 669
- Pedler, A., Ghataure, H. S., Davies, R. D., Harrison, B. A., Perley, R., Crane, P. C., & Unger, S. W. 1990, MNRAS, 246, 477
- Perucho, M., & Martí, J. M. 2002, ApJ, 568, 639
- Phillips, R. B., & Mutel, R. L. 1982, A&A, 106, 21
- Pihlström, Y. M., Conway, J. E., & Vermeulen, R. C. 2003, A&A, in press (astro-ph/0304305)
- Readhead, A. C. S., Taylor, G. B., Xu, W., Pearson, T. J., Wilkinson, P. N., & Polatidis, A. G. 1996, ApJ, 460, 612
- Rice, W., Lonsdale, Carol J., Soifer, B. T., Neugebauer, G., Koplan, E. L., Lloyd, L. A., de Jong, T., & Habing, H. J. 1988, ApJS, 68, 91
- Rickard, L. J., & Harvey, P. M. 1984, AJ, 89, 1520
- Rodgers, A. W., Conroy, P., & Bloxham, G. 1988, PASP, 100, 626
- Rodgers, A. W., Bloxham, G., & Conroy, P. 1993, PASP, 105, 315
- Rowan-Robinson, M. 2000, MNRAS, 316, 885
- Roy, A. L., & Norris, R. P. 1997, MNRAS, 289, 824
- Rush, B., Malkan, M. A., & Spinoglio, L. 1993, ApJS, 89, 1
- Sadler, E. M. 1984, AJ, 89, 53
- Sadler, E. M., Jenkins, C. R., & Kotanyi, C. G. 1989, MNRAS, 240, 591

- Saikia, D. J., & Salter, C. J. 1988, *ARA&A*, 26, 93
- Sanders, D. B., & Mirabel, I. F. 1985, *ApJ*, 298, L31
- Sanders, D. B., & Mirabel, I. F. 1996, *ARA&A*, 34, 749
- Sanders, D. B., Scoville, N. Z., Young, J. S., Soifer, B. T., Schloerb, F. P., Rice, W. L., & Danielson, G. E. 1986, *ApJ*, 305, L45
- Sanders, D. B., Soifer, B. T., Elias, J. H., Madore, B. F., Matthews, K., Neugebauer, G., & Scoville, N. Z. 1988a, *ApJ*, 325, 74
- Sanders, D. B., Soifer, B. T., Elias, J. H., Neugebauer, G., & Matthews, K. 1988b, *ApJ*, 328, L35
- Sanders, D. B., Soifer, B. T., Scoville, N. Z., & Sargent, A. I. 1988c, *ApJ*, 324, L55
- Sanders, D. B., Phinney, E. S., Neugebauer, G., Soifer, B. T., & Matthews, K. 1989, *ApJ*, 347, 29
- Sault, R. J., Teuben, P. J., & Wright, M. C. H. 1995, in *ASP Conf. Ser. 77, Astronomical Data Analysis Software & Systems IV*, ed. R. Shaw, H. E. Payne, & J. J. E. Hayes (San Francisco: ASP), 433
- Schmitt, H. R., Antonucci, R. R. J., Ulvestad, J. S., Kinney, A. L., Clarke, C. J., & Pringle, J. E. 2001, *ApJ*, 555, 663
- Scoville, N. Z., et al. 2000, *AJ*, 119, 991
- Shen, Z.-Q., et al. 1997, *AJ*, 114, 1999
- Shuder, J. M., & Osterbrock, D. E. 1981, *ApJ*, 250, 55
- Slee, O. B., Sadler, E. M., Reynolds, J. E., & Ekers, R. D. 1994, *MNRAS*, 269, 928
- Smith, E. P., & Kassim, N. E. 1993, *AJ*, 105, 46
- Snellen, I. A. G., Schilizzi, R. T., & van Langevelde, H. J. 2000a, *MNRAS*, 319, 429
- Snellen, I. A. G., Schilizzi, R. T., Miley, G. K., de Bruyn, A. G., Bremer, M. N., & Rottgering, H. J. A. 2000b, *MNRAS*, 319, 445
- Soifer, B. T., Houck, J. R., & Neugebauer, G. 1987, *ARA&A*, 25, 187
- Soifer, B. T., Boehmer, L., Neugebauer, G., & Sanders, D. B. 1989, *AJ*, 98, 766
- Sopp, H. M., & Alexander, P. 1991, *MNRAS*, 251, 14p
- Spencer, R. E., McDowell, J. C., Charlesworth, M., Fanti, C., Parma, P., & Peacock, J. A. 1989, *MNRAS*, 240, 657
- Stanghellini, C., O’Dea, C. P., Dallacasa, D., Baum, S. A., Fanti, R., & Fanti, C. 1998, *A&AS*, 131, 303
- Stockton, A., & Ridgway, S. E. 1991, *AJ*, 102, 488
- Tadhunter, C., Wills, K., Morganti, R., Oosterloo, T., & Dickson, R. 2001, *MNRAS*, 327, 227
- Thean, A., Pedlar, A., Kukula, M. J., Baum, S. A., & O’Dea, C. P. 2000, *MNRAS*, 314, 573
- Tran, Q. D., et al. 2001, *ApJ*, 552, 527
- Ulvestad, J. S. 1986, *ApJ*, 310, 136
- Ulvestad, J. S., & Ho, L. C. 2001, *ApJ*, 558, 561
- Ulvestad, J. S., & Wilson, A. S. 1983, *ApJ*, 264, L7
- Vader, J. P., Frogel, J. A., Terndrup, D. M., & Heisler, C. A. 1993, *AJ*, 106, 1743
- van Breugel, W. 1983, in *IAU Symposium 110, VLBI and Compact Radio Sources*, ed. R. Fanti, K. Kellerman, & G. Setti (Dordrecht: Reidel), 59
- van der Kruit, P. C. 1973, *A&A*, 29, 263
- Veilleux, S., Sanders, D. B., & Kim, D.-C. 1997, *ApJ*, 484, 92
- Véron, P. 1978, *Nature*, 272, 430
- Véron-Cetty, M.-P., Woltjer, L., Ekers, R. D., & Staveley-Smith, L. 1995, *A&A*, 297, L79
- Walker, R. C., Benson, J. M., & Unwin, S. C. 1987, *ApJ*, 316, 546
- Walsh, D. E. P., Knapp, G. R., Wrobel, J. M., & Kim, D. W. 1989, *ApJ*, 337, 209
- Wasilewski, A. J. 1981, *PASP*, 93, 560
- Wehrle, A. E., Cohen, M. H., Unwin, S. C., Aller, H. D., Aller, M. F., & Nicolson, G. 1992, *ApJ*, 391, 589
- Wilkinson, P. N., Tzioumis, A. K., Benson, J. M., Walker, R. C., Simon, R. S., & Kahn, F. D. 1991, *Nature*, 352, 313
- Wright, A. E., Griffith, M. R., Burke, B. F., & Ekers, R. D. 1994, *ApJS*, 91, 111
- Wright, A. E., Griffith, M. R., Hunt, A. J., Troup, E., Burke, B. F., & Ekers, R. D. 1996, *ApJS*, 103, 145
- Wunderlich, E., Klein, U., & Wielebinski, R. 1987, *A&AS*, 69, 487
- Xu, C., Baum, S. A., O’Dea, C. P., Wrobel, J. M., & Condon, J. J. 2000, *AJ*, 120, 2950
- Yun, M. S., Reddy, N. A., & Condon, J. J. 2001, *ApJ*, 554, 803
- Zheng, Z., Wu, H., Mao, S., Xia, X.-Y., Deng, Z.-G., & Zou, Z.-L. 1999, *A&A*, 349, 735

This figure "Drake.fig3a.gif" is available in "gif" format from:

<http://arxiv.org/ps/astro-ph/0306573v1>

This figure "Drake.fig3b.gif" is available in "gif" format from:

<http://arxiv.org/ps/astro-ph/0306573v1>

This figure "Drake.fig3c.gif" is available in "gif" format from:

<http://arxiv.org/ps/astro-ph/0306573v1>

This figure "Drake.fig3d.gif" is available in "gif" format from:

<http://arxiv.org/ps/astro-ph/0306573v1>

This figure "Drake.fig4.gif" is available in "gif" format from:

<http://arxiv.org/ps/astro-ph/0306573v1>

This figure "Drake.fig5.gif" is available in "gif" format from:

<http://arxiv.org/ps/astro-ph/0306573v1>